

样式定义：标题 2：段落间距段前：12 磅，段后：12 磅，行距：单倍行距，孤行控制，与下段同页

1 **Technical note: Applicability of physics-based and machine-learning-based**  
2 **algorithms of geostationary satellite in retrieving the diurnal cycle of cloud base**  
3 **height**

4  
5 Mengyuan Wang<sup>1</sup>, Min Min<sup>1\*</sup>, Jun Li<sup>2</sup>, Han Lin<sup>3</sup>, Yongen Liang<sup>1</sup>, Binlong Chen<sup>2</sup>,  
6 Zhigang Yao<sup>4</sup>, Na Xu<sup>2</sup>, Miao Zhang<sup>2</sup>

7  
8  
9 <sup>1</sup>School of Atmospheric Sciences, Southern Marine Science and Engineering  
10 Guangdong Laboratory (Zhuhai), and Guangdong Province Key Laboratory for  
11 Climate Change and Natural Disaster Studies, Zhuhai 519082, China

12 <sup>2</sup>Key Laboratory of Radiometric Calibration and Validation for Environmental  
13 Satellites and Innovation Center for FengYun Meteorological Satellite (FYSIC),  
14 National Satellite Meteorological Center (National Center for Space Weather), China  
15 Meteorological Administration, Beijing 100081, China

16 <sup>3</sup>Key Laboratory of Spatial Data Mining and Information Sharing of Ministry of  
17 Education, National and Local Joint Engineering Research Center of Satellite  
18 Geospatial Information Technology, Fuzhou University, Fuzhou 350108, China

19 <sup>4</sup>Beijing Institute of Applied Meteorology, Beijing 100029, China

20  
21  
22  
23 *Correspondence to:* Min Min (minm5@mail.sysu.edu.cn)

34

35 **Abstract.** Two groups of retrieval algorithms, one physics-based and the other  
36 machine-learning (ML) based, each consisting of two independent approaches, have  
37 been developed to retrieve cloud base height (CBH) and its diurnal cycle from  
38 Himawari-8 geostationary satellite observations. Validations have been conducted  
39 using the joint CloudSat/CALIOP (Cloud-Aerosol Lidar with Orthogonal Polarization)  
40 CBH products in 2017, ensuring independent assessments. Results show that the two  
41 ML-based algorithms exhibit markedly superior performance (the optimal method is  
42 with a correlation coefficient of  $R > 0.91$  and an absolute bias of approximately 0.8  
43 km) compared to the two physics-based algorithms. However, validations based on  
44 CBH data from the ground-based lidar at the Lijiang station in Yunnan province and  
45 the cloud radar at the Nanjiao station in Beijing, China, explicitly present  
46 contradictory outcomes ( $R < 0.60$ ). An identifiable issue arises with significant  
47 underestimations in the retrieved CBH by both ML-based algorithms, leading to an  
48 inability to capture the diurnal cycle characteristics of CBH. The strong consistence  
49 observed between CBH derived from ML-based algorithms and the spaceborne active  
50 sensor may be attributed to utilizing the same dataset for training and validation,  
51 sourced from the CloudSat/CALIOP products. In contrast, the CBH derived from the  
52 optimal physics-based algorithm demonstrates the good agreement in diurnal  
53 variations of CBH with ground-based lidar/cloud radar observations during the  
54 daytime (with an  $R$  value of approximately 0.7). Therefore, the findings in this  
55 investigation from ground-based observations advocate for the more reliable and  
56 adaptable nature of physics-based algorithms in retrieving CBH from geostationary  
57 satellite measurements. Nevertheless, under ideal conditions, with an ample dataset of  
58 spaceborne cloud profiling radar observations encompassing the entire day for  
59 training purposes, the ML-based algorithms may hold promise in still delivering  
60 accurate CBH outputs.

61 **Key words:** Geostationary meteorological satellite; cloud base height; physics-based  
62 algorithm; machine learning.

63

删除了: Four distinct

设置了格式: 字体: (默认) Times New Roman, (中文)  
DengXian, 小四, 字体颜色: 文字 1

设置了格式: 字体: (默认) Times New Roman, (中文)  
DengXian, 小四, 字体颜色: 文字 1

删除了: retrieval algorithms, comprising two physics-based  
and two machine-learning (ML) approaches, have been  
developed to retrieve cloud base height (CBH) and its diurnal  
cycle from Himawari-8 geostationary satellite observations...

69 **1 Introduction**

70 Clouds, comprising visible aggregates like atmospheric water droplets,  
71 supercooled water droplets, ice crystals, etc., cover roughly 70% of the Earth's surface  
72 (Stubenrauch et al., 2013). They play a pivotal role in global climate change, the  
73 hydrologic cycle, aviation safety, and serve as a primary focus in weather  
74 forecasting and climate research, particularly storm clouds (Hansen, 2007; Hartmann  
75 and Larson, 2002). From advanced geostationary (GEO) and polar-orbiting (LEO,  
76 low earth orbit) satellite imagers, various measurable cloud properties, such as cloud  
77 fraction, cloud phase, cloud top height (CTH), and cloud optical thickness (COT or  
78 D<sub>cot</sub>), are routinely retrieved. However, the high-quality cloud geometric height  
79 (CGH) and cloud base height (CBH), a fundamental macro physical parameter  
80 delineating the vertical distribution of clouds, remains relatively understudied and  
81 underreported. Nonetheless, for boundary-layer clouds, the cloud base height stands  
82 as a critical parameter depending on other cloud-controlling variables. These variables  
83 encompass the cloud-base temperature (Zhu et al., 2014), cloud-base vertical velocity  
84 (Zheng et al., 2020), activation of CCN (Cloud Condensation Nuclei) at the  
85 cloud-base (Rosenfeld et al., 2016; Miller et al., 2023), and the cloud-surface  
86 decoupling state (Su et al., 2022). These factors significantly impact convective cloud  
87 development and ultimately the climate. As well known, there are distinct diurnal  
88 cycle characteristics of clouds in different regions across the globe (Li et al., 2022).  
89 These diurnal cycle characteristics primarily stem from the daily solar energy cycle  
90 absorbed by both the atmosphere and Earth's surface. Besides, vertical atmospheric  
91 motions are shaped by imbalances in atmospheric heating and surface configurations,  
92 also leading to a range of cloud movements and structures (Miller et al., 2018). Cloud  
93 base plays a pivotal role in weather and climate processes. It is critical for predicting  
94 fog and cloud-related visibility issues important in aviation and weather forecasting.  
95 For instance, lower cloud bases often lead to more intense rainfall. In climate  
96 modeling, CBH is integral for accurate long-term weather predictions and  
97 understanding the radiative balance of the Earth, which influences global  
98 temperatures (Zheng and Rosenfeld, 2015). Hence, the accurate determination of  
99 CBH and its diurnal cycle with high spatiotemporal resolution becomes very  
100 important, necessitating comprehensive investigations (Viúdez-Mora et al., 2015;

删除了: depth

删除了: (Li et al., 2022)

删除了: spatial-temporal

104 Wang et al., 2020). Such efforts can provide deeper insights into potential  
105 ramifications of clouds on radiation equilibrium and global climate systems.

106 However, as one of the most crucial cloud physical parameters in atmospheric  
107 physics, the CBH poses challenges in terms of measurement or estimation from space.  
108 Presently, the primary methods for measuring CBH rely on ground-based  
109 observations, utilizing tools such as sounding balloons, Mie-scattering lidars,  
110 stereo-imaging cloud-height detection technologies, and cloud probe sensors  
111 (Forsythe et al., 2000; Hirsch et al., 2011; Seaman et al., 2017; Zhang et al., 2018;  
112 Zhou et al., 2019; Zhou et al., 2024). While *in-situ* ground-based observation methods  
113 offer highly accurate, reliable, and timely continuous CBH results, they are  
114 constrained by localized observation coverage and the sparse distribution of  
115 observation sites (Aydin and Singh, 2004). In recent decades, with the rapid  
116 advancement of meteorological satellite observation technology, spaceborne  
117 observing methods have emerged that provide global cloud observations with high  
118 spatiotemporal resolution compared to conventional ground-based remote sensing  
119 methods. In this realm, satellite remote sensing techniques for measuring CBH fall  
120 primarily into two categories: active and passive methods. Advanced active remote  
121 sensing technologies like CloudSat ([Stephens et al., 2002](#)) and Cloud-Aerosol Lidar  
122 and Infrared Pathfinder Satellite Observation (CALIPSO) ([Winker et al., 2009](#)) in the  
123 National Aeronautics and Space Administration (NASA) A-Train ([Afternoon-Train](#))  
124 series ([Stephens et al., 2002](#)) can capture global cloud profiles, including CBH, with  
125 high quality by detecting unique return signals from cloud layers using onboard active  
126 millimeter wave radar or lidar. However, their viewing footprints are limited along the  
127 nadir of the orbit, implying that observation coverage remains confined primarily to a  
128 horizontal scale (Min et al., 2022; Lu et al., 2021).

129 In addition to active remote sensing methods, satellite-based passive remote  
130 sensing technologies can also play an important role in estimating CBH (Meerkötter  
131 and Bugliaro, 2009; Lu et al., 2021). As well known, the physics-based principles and  
132 retrieval methods for CTH have reached maturity and are now widely employed in  
133 satellite passive remote sensing field (Heidinger and Pavolonis, 2009; Wang et al.,  
134 2022). However, the corresponding physical principles or methods for measuring  
135 CBH using satellite passive imager measurements are still not entirely clear and  
136 unified (Heidinger et al., 2019; Min et al., 2020). A recent study by Yang et al. ([2021](#))  
137 utilized oxygen A-band data observed by the Orbiting Carbon Observatory 2 (OCO-2)

删除了: spatio-temporal

删除了: (Stephens et al., 2002)

删除了: (Winker et al., 2009)

删除了: (Stephens et al., 2002)

删除了: cloud top height (

删除了: )

删除了: (

删除了: ,

146 to retrieve single-layer marine liquid CBH. These methods aforementioned are  
147 prominent in retrieving CBH through passive space-based remote sensing techniques.  
148 The first method involves the extrapolation technique for retrieving CBH for clouds  
149 of the same type. For instance, Wang et al. (2012) proposed a method to extrapolate  
150 CBH from CloudSat using spatiotemporally matched MODIS (Moderate Resolution  
151 Imaging Spectroradiometer) cloud classification data. The second physics-based  
152 retrieval method first approximates the cloud geometric thickness using its optical  
153 thickness. It then employs the previously derived CTH product to compute the  
154 corresponding CBH using the respective NOAA (National Oceanic and Atmospheric  
155 Administration) SNPP/VIIRS (Suomi National Polar-orbiting Partnership/Visible  
156 Infrared Imaging Radiometer Suite) products (Noh et al., 2017). Hutchison et al.  
157 (2002 and 2006) also formulated an empirical algorithm that estimates both cloud  
158 geometric thickness (CGT) and CBH. This algorithm relies on statistical analyses  
159 derived from MODIS COT and cloud liquid water path products (Hutchison et al.,  
160 2006; Hutchison, 2002).

161 Machine learning (ML) has proven to be highly effective in addressing nonlinear  
162 problems within remote sensing and meteorology fields, such as precipitation  
163 estimation and CTH retrieval (Min et al., 2020; HåKansson et al., 2018; Kühnlein et  
164 al., 2014). In recent years, several studies have leveraged ML-based algorithms to  
165 retrieve CBH, establishing nonlinear connections between CBH and GEO satellite  
166 observations. For instance, Tan et al. (2020) integrated CTH and cloud optical  
167 properties products from Fengyun-4A (FY-4A) GEO satellite with spatiotemporally  
168 matched CBH data from CALIPSO/CloudSat. They developed a random forest (RF)  
169 model for CBH retrieval. Similarly, Lin et al. (2022) constructed a gradient boosted  
170 regression tree (GBRT) model using U.S. new-generation Geostationary Operational  
171 Environmental Satellites-R Series (GOES-R) Advanced Baseline Imager (ABI) level  
172 1B radiance data and the ERA5 (the fifth generation ECMWF) reanalysis dataset  
173 (<https://cds.climate.copernicus.eu/cdsapp#!/search?type=dataset>). They employed  
174 CALIPSO CBH data as labels to achieve single-layer CBH retrievals. Notably, the  
175 CBH quality of ML-based algorithms was found to surpass that of physics-based  
176 algorithms (Lin et al., 2022). Moreover, Tana et al. (2023) utilized Himawari-8 data  
177 and the random forest algorithm to develop a novel CBH algorithm, achieving a high  
178 correlation coefficient (R) of 0.92 and a low root mean square error (RMSE) of 1.17  
179 km.

删除了: wo primary

删除了:(

删除了:,

删除了: spatial-temporally

删除了: correlated

删除了: cloud optical thickness

删除了: previous

删除了: spatial-temporal

删除了: (Tan et al., 2020)

删除了: (Lin et al., 2022)

删除了: (Tana et al., 2023)

191 However, these former studies did not discuss whether both physics-based and  
192 ML-based algorithms of GEO satellite could retrieve the diurnal cycle of CBH well.  
193 This gap in research could be mainly attributed to potential influences from the fixed  
194 LEO satellite (with active radar or lidar) passing time in the previous CBH retrieval  
195 model (Lin et al., 2022). Hence, it is crucial to thoroughly investigate the diurnal  
196 cycle features of CBH derived from GEO satellite measurements by comparing them  
197 with ground-based radar and lidar observations (Min and Zhang, 2014; Warren and  
198 Eastman, 2014). In this study, we aim to assess the applicability and feasibility of  
199 both physics-based and ML-based algorithms of GEO satellites in capturing the  
200 diurnal cycle characteristics of CBH.

201 The subsequent sections of this paper are structured as follows. Section 2  
202 provides a concise overview of the data employed in this study. Following that,  
203 section 3 introduces the four distinct physics/ML-based CBH retrieval algorithms. In  
204 section 4, the CBH results obtained from these four algorithms are analyzed, and  
205 comparisons are drawn with spatiotemporally matched CBHs from ground-based  
206 cloud radar and lidar. Finally, section 5 encapsulates the primary conclusions and new  
207 findings derived from this study.

## 208 2 Data

209 In this study, observations from the Himawari-8 (H8) Advanced Himawari  
210 Imager (AHI) are utilized for the retrieval of high spatiotemporal resolution CBH.  
211 Launched successfully by the Japan Meteorological Administration on October 7,  
212 2014, the H8 geostationary satellite is positioned at 140.7°E. The AHI onboard H8  
213 encompasses 16 spectral bands ranging from 0.47  $\mu\text{m}$  to 13.3  $\mu\text{m}$ , featuring spatial  
214 resolutions of 0.5–2 km. This includes 3 visible (VIS) bands at 0.5–1 km, 3  
215 near-infrared (NIR) bands at 1–2 km, and 10 infrared (IR) bands at 2 km. The  
216 H8/AHI can scan a full disk area within 10 minutes, two specific areas within 2.5  
217 minutes, a designated area within 2.5 minutes, and two landmark areas within 0.5  
218 minutes (Iwabuchi et al., 2018). Its enhanced temporal resolution and observation  
219 frequency facilitate the tracking of rapidly changing weather systems, enabling the  
220 accurate determination of quantitative atmospheric parameters (Bessho et al., 2016).

221 Operational H8/AHI Level-1B data, accessible from July 7, 2015, are freely  
222 available on the satellite product homepage of the Japan Aerospace Exploration

删除了: As well known, there are distinct diurnal cycle characteristics of clouds in different regions across the globe (Li et al., 2022). These diurnal cycle characteristics primarily stem from the daily solar energy cycle absorbed by both the atmosphere and Earth's surface. Besides, vertical atmospheric motions are shaped by imbalances in atmospheric heating and surface configurations, also leading to a range of cloud movements and structures (Miller et al., 2018). Cloud base plays a pivotal role in weather and climate processes. It is critical for predicting fog and cloud-related visibility issues important in aviation and weather forecasting. For instance, lower cloud bases often lead to more intense rainfall. In climate modeling, CBH is integral for accurate long-term weather predictions and understanding the radiative balance of the Earth, which influences global temperatures (Zheng and Rosenfeld, 2015). ...

删除了: spatially and temporal

删除了: s

241 Agency (Letu et al., 2019). The Level-2 cloud products utilized in this study,  
242 including cloud mask (CLM), CTH, cloud effective particle radius (CER or  $R_{eff}$ ), and  
243 COT, are generated by the Fengyun satellite science product algorithm testbed  
244 (FYGAT) (Wang et al., 2019; Min et al., 2017) of the China Meteorological  
245 Administration (CMA) for various applications. It is important to note that certain  
246 crucial preliminary cloud products, such as CLM, have been validated in prior studies  
247 (Wang et al., 2019; Liang et al., 2023). Nevertheless, before initiating CBH retrieval,  
248 it is imperative to validate the H8/AHI cloud optical and microphysical products from  
249 the FYGAT retrieval system. This validation is carried out by using analogous  
250 MODIS Level-2 cloud products as a reference. Additional details regarding the  
251 validation of cloud products are provided in the Appendix A section.

252 In addition to the H8/AHI Level-1/2 data, the Global Forecast System (GFS)  
253 numerical weather prediction (NWP) data are employed for CBH retrieval in this  
254 study. The variables include land/sea surface temperature and the vertical profiles of  
255 temperature, humidity, and pressure. Operated by the U.S. NOAA (Kalnay et al.,  
256 1996), the GFS serves as a global and advanced NWP system. The operational GFS  
257 system routinely delivers global, high-quality and gridded NWP data at 3-hour  
258 intervals, with four different initial forecast times per day (00:00, 06:00, 12:00, and  
259 18:00 UTC). The three-dimensional NWP data cover the Earth in a  $0.5^\circ \times 0.5^\circ$  grid  
260 interval and resolve the atmosphere with 26 vertical levels from the surface (1000 hPa)  
261 up to the top of the atmosphere (10 hPa).

262 As previously mentioned, the official MODIS Collection-6.1 Level-2 cloud  
263 product Climate Data Records (Platnick et al., 2017) are utilized in this study to  
264 validate the H8/AHI cloud products (CTH, CER, and COT) generated by the FYGAT  
265 system. MODIS sensors are onboard NASA Terra and Aqua polar-orbiting satellites.  
266 Terra functions as the morning satellite, passing through the equator from north to  
267 south at approximately 10:30 local time, while Aqua serves as the afternoon satellite,  
268 traversing the equator from south to north at around 13:30 local time. As a successor  
269 to the NOAA Advanced Very High Resolution Radiometer (AVHRR), MODIS  
270 features 36 independent spectral bands and a broad spectral range from 0.4  $\mu\text{m}$  (VIS)  
271 to 14.4  $\mu\text{m}$  (IR), with a scanning width of 2330 km and spatial resolutions ranging  
272 from 0.25 to 1.0 km. Recent studies (Baum et al., 2012; Platnick et al., 2017) have  
273 highlighted significant improvements and collective changes in cloud top, optical, and  
274 microphysical properties from Collection-5 to Collection-6.

删除了: cloud optical thickness (

删除了: )

删除了: the

删除了: cloud mask

删除了: ly

280 In addition to the passive spaceborne imaging sensors mentioned above, the  
281 CloudSat satellite, equipped with a 94-GHz active cloud profiling radar (CPR), holds  
282 the distinction of being the first sun-synchronous orbit satellite specifically designed  
283 to observe global cloud vertical structures and properties. It is part of the A-Train  
284 series of satellites, akin to the Aqua satellite, launched and operated by NASA  
285 (Heymsfield et al., 2008). CALIPSO is another polar-orbiting satellite within the  
286 A-Train constellation, sharing an orbit with CloudSat and trailing it by a mere 10–15  
287 seconds. CALIPSO is the first satellite equipped with an active dual-channel CALIOP  
288 at 532 and 1064 nm bands (Hunt et al., 2009). Both CloudSat and CALIPSO possess  
289 notable advantages over passive spaceborne sensors due to the 94-GHz radar of  
290 CloudSat and the joint return signals of lidar and radar on CALIPSO. These features  
291 enhance their sensitivity to optically thin cloud layers and ensure strong penetration  
292 capability, resulting in more accurate CTH and CBH detections compared to passive  
293 spaceborne sensors (CAL\_LID\_L2\_05kmCLay-Standard-V4-10). The joint cloud  
294 type products of 2B-CLDCLASS-LIDAR, derived from both CloudSat and CALIPSO  
295 measurements, offer a comprehensive description of cloud vertical structure  
296 characteristics, cloud type, CTH, CBH, etc. The time interval between each profile in  
297 this product is approximately 3.1 seconds, and the horizontal resolution is 2.5 km  
298 (along track)×1.4 km (cross-track). Each profile is divided into 125 layers with a  
299 240-m vertical interval. For more details on 2B-CLDCLASS-LIDAR products, please  
300 refer to the CloudSat official product manual (Sassen and Wang, 2008). In this study,  
301 we consider the lowest effective cloud base height from the joint CloudSat/CALIOP  
302 data as the true values for training and validation. Please note that for this study, we  
303 utilized one-year H8/AHI data and matched it with the joint CloudSat/CALIOP data  
304 from January 1 to December 31 of 2017.

### 305 3 Physics/machine-learning based cloud-base height algorithms

#### 306 3.1 GEO Cloud-base height retrieval algorithm from the interface data 307 processing segment of the Visible Infrared Imaging Radiometer Suite

308 The Joint Polar Satellite System (JPSS) program is a collaborative effort between  
309 NASA and NOAA. The operational CBH retrieval algorithm, part of the 30  
310 Environmental Data Records (EDR) of JPSS, can be implemented operationally  
311 through the Interface Data Processing Segment (IDPS) (Baker, 2011). In this study,

删除了: (Afternoon-Train)

设置了格式: 字体: (默认) Times New Roman, (中文) DengXian, 小四, 字体颜色: 文字 1

设置了格式: 字体: (中文) DengXian

设置了格式: 字体: (默认) Times New Roman, (中文) DengXian, 小四, 字体颜色: 文字 1

313 our geostationary satellite CBH retrieval algorithm aligns with the IDPS CBH  
314 algorithm developed by (Baker, 2011). Utilizing the geostationary H8/AHI cloud  
315 products discussed earlier, this new GEO CBH retrieval algorithm is succinctly  
316 outlined below. ▼

317 The new GEO IDPS CBH algorithm initiates the process by first retrieving the  
318 CGT from bottom to top. Subsequently, CGT is subtracted from the corresponding  
319 CTH to calculate CBH ( $CBH = CTH - CGT$ ). The algorithm is divided into two  
320 independent executable modules based on cloud phase, distinguishing between liquid  
321 water and ice clouds. CBH of water cloud retrieval requires COT and CER as inputs.  
322 For ice clouds, an empirical equation is employed for CBH retrieval. However, the  
323 standard deviations of error in IDPS CBH for individual granules often exceed the  
324 JPSS VIIRS minimum uncertainty requirement of  $\pm 2\text{km}$  (Noh et al., 2017). The  
325 accuracy of IDPS algorithm-derived CBHs can be directly affected by several factors,  
326 including cloud optical thickness, cloud effective particle size, the presence of  
327 multi-layered cloud systems, lack of solar illumination, and highly reflective surfaces  
328 such as snow or ice surfaces. For a more comprehensive understanding of this CBH  
329 algorithm, please refer to the IDPS algorithm documentation (Baker, 2011). Note that,  
330 similar to previous studies on cloud retrieval (Noh et al., 2017; Platnick et al., 2017),  
331 this investigation also assumes a single-layer cloud for all CBH algorithms, due to the  
332 challenges associated with determining multilayer cloud structures.

### 333 3.2 GEO Cloud-base height retrieval algorithm implemented in the Clouds from 334 Advanced Very High Resolution Radiometer Extended system

335 As mentioned above, the accuracy of the GEO IDPS algorithm is highly  
336 dependent on the initial input parameters such as cloud phase,  $D_{COT}$  and  $R_{eff}$ , which  
337 may introduce some uncertainties in the final retrieval results. In contrast, a more  
338 reliable statistically-based algorithm is proposed and implemented here, which is  
339 named the GEO CLAVR-x (Clouds from AVHRR Extended, NOAA's operational  
340 cloud processing system for the AVHRR) CBH algorithm (Noh et al., 2017), and it  
341 mainly refers to NOAA AWG CBH algorithm (ACBA) (Noh et al., 2022). Previous  
342 studies have also demonstrated a  $R$  of 0.569 and a RMSE of 2.3 km for the JPSS  
343 VIIRS CLAVR-x CBH algorithm. It is anticipated that this algorithm will also be  
344 employed for the NOAA GOES-R geostationary satellite imager (Noh et al., 2017;  
345 Seaman et al., 2017).

删除了: ↓

删除了: cloud geometric thickness (

删除了: )

删除了: cloud top height (

删除了: )

删除了: Cloud Optical Thickness (

删除了: or  $D_{COT}$ )

删除了: Effective Radius (

删除了: or  $R_{eff}$ )

删除了: ple

设置了格式: 字体颜色: 文字 1

设置了格式: 字体颜色: 文字 1

设置了格式: 字体颜色: 文字 1

删除了: (Noh et al., 2017)

删除了: (Noh et al., 2022)

删除了: correlation coefficient

删除了: root mean square error (

删除了: )

删除了: R

362 Similar to the GEO IDPS CBH retrieval algorithm mentioned earlier, the GEO  
363 CLAVR-x CBH retrieval algorithm also initially obtains CGT and CTH, subsequently  
364 calculating CBH by subtracting CGT from CTH (CTH–CGT). However, the specific  
365 calculation method for the CGT value differs. This algorithm is suitable for  
366 single-layer and the topmost layer of multi-layer clouds, computing CBH using the  
367 CTH at the top layer of the cloud. In comparison with the former GEO IDPS CBH  
368 algorithm, the GEO CLAVR-x CBH algorithm considers two additional cloud types:  
369 deep convection clouds and thin cirrus clouds. For more details on this CLAVR-x  
370 CBH algorithm, please refer to the original algorithm documentation (Noh et al.,  
371 2017).

删除了: This algorithm is suitable for both single-layer and  
multi-layer clouds, computing CBH using the CTH at the top

### 372 3.3 Random-forest-based cloud-base height estimation algorithm

373 RF, one of the most significant ML algorithms, was initially proposed and  
374 developed by (Breiman, 2001). It is widely employed to address classification and  
375 regression problems based on the law of large numbers. The law of large numbers  
376 states that when independent and identically distributed random experiments are  
377 repeatedly conducted, the average of the results will converge to the expected value as  
378 the number of trials increases. In RF algorithms, it primarily serves to increase  
379 randomness and independence in model construction, thus enhancing the model's  
380 stability and generalizability. Here, the RF method utilizes a forest of trees, serving as  
381 an integrated algorithm that enhances overall model accuracy and generalization by  
382 combining multiple weak classifiers. The final prediction is calculated through voting  
383 or averaging. The RF method is well-suited for capturing complex or nonlinear  
384 relationships between predictors and predictands. As mentioned earlier, this statistical  
385 or ML-based algorithm has been already proven successful in retrieving CTH and  
386 CBH (Min et al., 2020; Tan et al., 2020).

387 In this study, two distinct ML-based GEO CBH algorithms, namely VIS+IR and  
388 IR-single (only uses observations of H8/AHI IR channels), are devised to retrieve or  
389 predict the CBH using different sets of predictors. The RF training of the chosen  
390 predictors is formulated as follows:

$$391 \text{CBH} = RF_{\text{reg}}[x_1, x_2, \dots, x_n], \quad (1)$$

392 where  $RF_{\text{reg}}$  denotes the regression Random Forest model, and  $x_i$  represents the  $i$ th  
393 predictor. The selected predictors from H8/AHI for both the VIS+IR and IR RF  
394 model training and prediction are detailed in Table 1, mainly referencing Min et al.

删除了: s

398 (2020) and Tan et al. (2020). The VIS+IR algorithm retrieves CBH based on NWP  
399 data (atmospheric temperature and altitude profiles, total precipitable water (TPW),  
400 surface temperature), surface elevation, air mass 1 (air mass 1=1/cos(view zenith  
401 angle)), and air mass 2 (air mass 2=1/cos(solar zenith angle)). The rationale for  
402 choosing air mass and TPW is their ability to account for the potential absorption  
403 effect of water vapor along the satellite viewing angle. The predictors in CBH  
404 retrieval also include the IR band Brightness Temperature (BT) and VIS band  
405 reflectance. The IR-single algorithm selects the same Global Forecast System (GFS)  
406 NWP data as the VIS+IR algorithm but employs different view zenith angles and  
407 azimuth angles.

408 To optimize the RF prediction model, the hyperparameters of the RF model are  
409 tuned individually. The parameters and their dynamic ranges involved in tuning the  
410 RF prediction models include the number of trees [100, 200, 300, 400, 500], the  
411 maximum depth of trees [10, 20, 30, 40, 50], the minimum number of samples  
412 required to split an internal node [2, 4, 6, 8, 10], and the minimum number of samples  
413 required to be at a leaf node [1, 3, 5, 7, 9]. In this study, we set the smallest number of  
414 trees in the forest to 100 and the maximum depth of the tree to 40.

#### 415 3.4 Evaluation method

416 The performance of RF models and physics-based method will be assessed using  
417 mean absolute error (MAE), mean bias error (MBE), RMSE, R, and standard  
418 deviation (STD) scores based on the testing dataset. These scores mentioned above  
419 are used to understand different aspects of the predictive performance of model: MAE  
420 and RMSE provide insights into the average error magnitude, MBE indicates bias in  
421 the predictions, R evaluates the linear association between observed and predicted  
422 values, and STD assesses the variability of the predictions. In the RF IR-single  
423 algorithm, 581,783 matching points are selected from H8/AHI and CloudSat data for  
424 2017. Seventy percent of these points are randomly assigned to the training dataset,  
425 and the remainder serves as the testing dataset. For the RF VIS+IR algorithm, a total  
426 of 418,241 matching points are chosen, with 70% randomly allocated to the training  
427 set. Note that the reduced data amount is because only daytime data can be used for  
428 the VIS+IR method training. It's important to note that the two training datasets in

删除了: 3

设置了格式: 英语(英国)

带格式的: 标题 2, 缩进: 首行缩进: 0 厘米

删除了: root mean square error (

删除了: )

删除了: correlation coefficient

删除了: (

删除了: )

设置了格式: 字体: 非倾斜

435 CloudSat will also be used to verify the CBHs obtained by cloud radar and lidar. The  
436 statistical formulas for evaluation are as follows:

437  $MAE = \frac{1}{n} \sum_{i=1}^n |y_i - x_i|$ , (2)

438  $MBE = \frac{1}{n} \sum_{i=1}^n (y_i - x_i)$ , (3)

439  $RMSE = \sqrt{\frac{1}{n} \sum_{i=1}^n (y_i - x_i)^2}$ , (4)

440  $R = \frac{\sum_{i=1}^n (y_i - \bar{y})(x_i - \bar{x})}{\sqrt{\sum_{i=1}^n (y_i - \bar{y})^2} \sqrt{\sum_{i=1}^n (x_i - \bar{x})^2}}$ , (5)

441  $STD = \sqrt{\frac{1}{n-1} \sum_{i=1}^n (x_i - \bar{x})^2}$ , (6)

442 where  $n$  is the sample number,  $y_i$  is the  $i$ th CBH retrieval result, and  $x_i$  is the  $i$ th joint  
443 CloudSat/CALIOP CBH product.

444 Since the two RF models (VIS+IR and IR-single) select 230 typical variables to  
445 fit CBHs, the importance scores of these predictors in the two ML-based algorithms  
446 are ranked for better optimization. In a Random Forest model, feature importance  
447 indicates how much each input variable contributes to the model's predictive accuracy  
448 by measuring the decrease in impurity or error when the feature is used to split data  
449 (Gregorutti et al., 2017). In the VIS+IR model, the top-ranked predictors are CTH and  
450 cloud top temperature (CTT) from the H8/AHI Level-2 product (see Fig. B1 in  
451 Appendix B). It is important to note that  $D_{COT}$  is a crucial and sensitive factor for  
452 these ML-based algorithms. Retrieving CBH samples with relatively low  $D_{COT}$   
453 remains challenging due to the low signal-to-noise ratio when  $D_{COT}$  is low (Lin et al.,  
454 2022). To address this issue, samples with  $D_{COT}$  less than 1.6 are filtered in the  
455 VIS+IR model, and samples with relatively large BTs at Channel-14 are filtered in the  
456 IR-single model. This filtering process significantly improves the R value from 0.869  
457 to 0.922 in the VIS+IR model and from 0.868 to 0.911 in the IR-single model. For  
458 more details on the algorithm optimization, please refer to Appendix B.

## 459 4 Results and Discussions

### 460 4.1 Comparisons with the joint CloudSat/CALIPSO cloud-base height product

461 The H8/AHI satellite CBH data retrieved by the four algorithms are matched  
462 spatiotemporally with the 2B-CLDCLASS-LIDAR cloud product from joint

带格式的：缩进：首行缩进： 0.74 厘米

设置了格式：字体：(默认) Times New Roman, (中文) DengXian, 小四, 字体颜色：文字 1

设置了格式：字体：(默认) Times New Roman, (中文) DengXian, 小四, 字体颜色：文字 1

删除了：'

设置了格式：字体：倾斜

删除了：

删除了：s

删除了：patially and temporal

467 CloudSat/CALIPSO observations in 2017. In this process, the nearest distance  
468 matching method is employed, ensuring that the observation time difference between  
469 the CloudSat/CALIPSO observation point and the matched Himwari-8 data is less  
470 than 5 minutes (Noh et al., 2017). As in earlier study (Min et al., 2020), we also used  
471 70% of the matched data for training and 30% of an independent sample for  
472 validation. Figure 1 displays a comparison of CBH results over the full disk at 02:00  
473 UTC on January 1, 2017, retrieved by the GEO IDPS algorithm, the GEO CLAVR-x  
474 algorithm, the RF VIS+IR algorithm, and the RF IR-single algorithm. A similar  
475 distribution pattern and magnitude of CBHs retrieved by these four independent  
476 algorithms can be observed in Figure 1. However, notable differences exist between  
477 physics-based and ML-based algorithms. Further comparisons are conducted and  
478 analyzed with spaceborne and ground-based lidar and radar observations in the  
479 subsequent sections of this study.

#### 480 4.1.1 Joint scatter plots

481 Figure 2 presents the density scatter plot of the CBHs retrieved from the GEO  
482 IDPS and GEO CLAVR-x algorithms compared with the CBHs from the joint  
483 CloudSat/CALIPSO product, along with the related scores of MAE, MBE, RMSE,  
484 and R calculated and labeled in each panel. The calculated R exceeds the 95%  
485 significance level ( $p < 0.05$ ). For the GEO IDPS algorithm, the R is 0.62, the MAE is  
486 1.826 km, and the MBE and RMSE are -0.232 and 2.642 km (Fig. 2a). In comparison,  
487 Seaman et al. (2017) compared the operational VIIRS CBH product retrieved by the  
488 similar SNPP/VIIRS IDPS algorithm with the CloudSat CBH results. In their results,  
489 the R is 0.569, and the RMSE is 2.3 km. For the new GEO CLAVR-x algorithm (Fig.  
490 2b), the R is 0.647, and the RMSE is 2.91 km. The larger RMSE from two  
491 independent physics-based CBH algorithms demonstrate a slightly poorer  
492 performance and precision of these retrieval algorithms for GEO satellites.  
493 Particularly, the larger RMSEs (2.642 and 2.91 km) indicate weaker stabilities of the  
494 GEO IDPS and CLAVR-x CBH algorithms, compared with VIIRS CBH product  
495 (Seaman et al., 2017). In this figure, more samples can be found near the 1:1 line,  
496 implying the good quality of retrieved CBHs. However, in stark contrast, quite a  
497 number of CBH samples retrieved by both GEO IDPS and GEO CLAVR-x  
498 algorithms (compared with the official VIIRS CBH product) fall below 1.0 km,  
499 indicating relatively large errors when compared with the joint CloudSat/CALIPSO  
500 CBH product. Moreover, Figure 2 reveals that relatively large errors are also found in

设置了格式: 字体: (默认) Times New Roman, (中文) DengXian, 小四, 字体颜色: 文字 1

设置了格式: 字体: (默认) Times New Roman, (中文) DengXian, 小四, 字体颜色: 文字 1

设置了格式: 字体: (默认) Times New Roman, (中文) DengXian, 小四, 字体颜色: 文字 1

设置了格式: 字体: (默认) Times New Roman, (中文) DengXian, 小四, 字体颜色: 文字 1

设置了格式: 字体: (默认) Times New Roman, (中文) DengXian, 小四, 字体颜色: 文字 1

设置了格式: 字体: (默认) Times New Roman, (中文) DengXian, 小四, 字体颜色: 文字 1

设置了格式: 字体: (默认) Times New Roman, (中文) DengXian, 小四, 字体颜色: 文字 1

删除了: ..

删除了: ..

带格式的: 缩进: 首行缩进: 0 厘米

删除了: Fig. 2

删除了: (

删除了: ,

删除了: The poor predictive performance of physics-based  
algorithm for samples with a CBH lower than 1 km is likely  
due to insufficient cloud base information in the visible band  
observation data.

删除了: ..

511 the CBHs lower than 2 km for the four independent algorithms, primarily caused by  
512 the weak penetration ability of VIS or IR bands on thick and low clouds.

513 Referring to the joint CloudSat/CALIPSO CBH product, [Figures 2c and 2d](#) 删除了:..  
514 present the validations of the CBH results retrieved from two ML-based algorithms  
515 using the VIS+IR (only retrieving the CBH during the daytime) and IR-single models.  
516 [Figure 2c](#) demonstrates better consistency of CBH between the VIS+IR model and the 删除了:..  
517 joint CloudSat/CALIPSO product with  $R = 0.905$ ,  $MAE = 0.817$  km,  $MBE = 0.425$  删除了:..  
518 km, and  $RMSE = 1.706$  km. [Figure 2d](#) also displays a relatively high  $R$  of 0.876 when 删除了:..  
519 validating the IR-single model, with  $MAE = 0.882$ ,  $MBE = -0.445$ , and  $RMSE =$   
520 1.995. Therefore, both VIS+IR and IR-single models can obtain high-quality CBH  
521 retrieval results from geostationary imager measurements. In comparison, previous  
522 studies also proposed similar ML-based algorithms for estimating CBH using FY-4A  
523 satellite imager data. For example, (Tan et al., 2020) used the variables of CTH,  $D_{COT}$ ,  
524  $R_{eff}$ , cloud water path, longitude/latitude from FY-4A imager data to build the training  
525 and prediction model and obtained CBH with  $MAE = 1.29$  km and  $R = 0.80$ . In this  
526 study, except CTH, the other Level-2 products and geolocation data  
527 (longitude/latitude) used in (Tan et al., 2020) are abandoned, while the matched  
528 atmospheric profile products (such as temperature and relative humidity) from NWP  
529 data are added. These changes in ML-based model training and prediction lead to  
530 more accurate CBH retrieval results. Note that, in accordance with the previous study  
531 conducted by (Noh et al., 2017), we excluded CBH samples obtained from  
532 CloudSat/CALIPSO that were smaller than 1 km in our comparisons. This exclusion  
533 was primarily due to the presence of ground clutter contamination in the CloudSat  
534 CPR data (Noh et al., 2017).

#### 535 [4.1.2 Test case](#)

536 [Figure 3](#) displays two cross-sections of CBH from various sources overlaid with 删除了:..  
537 CloudSat radar reflectivity (unit: dBZ) for [spatiotemporally](#) matched cases. The 删除了:..  
538 periods covered are from 03:16 to 04:55 UTC on January 13, 2017 (154.0°E–160.0°E; 删除了:..  
539 40.56°S–53.39°S) and from 05:38 to 07:17 UTC on January 14, 2017 (107.1°E–  
540 107.8°E; 8.35°N–11.57°N). The CloudSat radar reflectivity and joint 删除了:..  
541 CloudSat/CALIPSO product provide insights into the vertical structure or distribution 删除了:..  
542 of clouds and their corresponding CBHs. The results from the four GEO CBH 删除了:..  
543 retrieval algorithms (GEO IDPS, GEO CLAVR-x, RF VIS+IR model, and RF 删除了:..  
544 IR-single model) mentioned earlier are individually marked with different markers in 删除了:..

550 each panel. According to Figure 3a, the GEO IDPS algorithm faces challenges in  
 551 accurately retrieving CBHs for geometrically thicker cloud samples near 157°E.  
 552 Optically thick mid- and upper-level cloud layers may obscure lower-level cloud  
 553 layers. However, the CBH results retrieved by the GEO IDPS algorithm near 155°E  
 554 (in Fig. 3a) and 107.4°E (in Fig. 3b) align with the joint CloudSat/CALIPSO CBH  
 555 product. It is worth noting that the inconsistency observed between 107.2°E and  
 556 107.3°E in Figure 3b, specifically regarding the CBHs around 1 km obtained from  
 557 CloudSat/CALIPSO, can likely be attributed to ground clutter contamination in the  
 558 CloudSat CPR data (Noh et al., 2017). The GEO CLAVR-x algorithm achieves  
 559 improved CBH results compared to the GEO IDPS algorithm. It can even retrieve  
 560 CBHs for some thick cloud samples that are invalid when using the GEO IDPS  
 561 algorithm. However, the CBHs from the GEO CLAVR-x algorithm are noticeably  
 562 higher than those from the joint CloudSat/CALIPSO product. In contrast, the CBHs  
 563 from the two ML-based algorithms show substantially better results than those from  
 564 the other two physics-based algorithms. Particularly, the ML-based VIS+IR model  
 565 algorithm yields the best CBH results. However, compared with those from the two  
 566 physics-based algorithms, the CBHs from the two ML-based algorithms still exhibit a  
 567 significant error around 5 km.

#### 568 4.2 Comparisons with the ground-based lidar and cloud radar measurements

569 Lidar actively emits lasers in different spectral bands into the air. When the laser  
 570 signal encounters cloud particles during transmission, a highly noticeable  
 571 backscattered signal is generated and received (Omar et al., 2009). When lidar  
 572 measures clouds, the intensity of the echo signal from the cloud to the laser satisfies  
 573 the lidar equation as follows:

$$574 P(r) = C * \beta(r) * r^{-2} * \exp[-2 \int_0^r \sigma(z) dz], \quad (7)$$

575 where  $P(r)$  is the intensity of the atmospheric backscattered signal received by the  
 576 laser telescope from the emission point in distance  $r$  (unit: Watt or W);  $C$  is the lidar  
 577 system instrumentation constant (unit:  $\text{W} \cdot \text{km}^3 \cdot \text{sr}$ );  $r$  is the detection distance (unit:  
 578 km);  $\beta(r)$  is the backscattering coefficient at the emission point in distance  $r$  (unit:  
 579  $\text{km}^{-1} \cdot \text{sr}^{-1}$ );  $\sigma(z)$  is the extinction coefficient at the distance emission point in distance  
 580  $z$  (unit:  $\text{km}^{-1}$ ). This return signal is markedly distinct from atmospheric aerosol  
 581 scattering signals and noise, making CBH easily obtainable from the signal difference

删除了: .

删除了: .

删除了: Since the two RF models (VIS+IR and IR-single) select 230 typical variables to fit CBHs, the importance scores of these predictors in the two ML-based algorithms are ranked for better optimization. In the VIS+IR model, the top-ranked predictors are CTH and cloud top temperature (CTT) from the H8/AHI Level-2 product (see Fig. B1 in Appendix B). It's important to note that  $D_{\text{COT}}$  is a crucial and sensitive factor for these ML-based algorithms. Retrieving CBH samples with relatively low  $D_{\text{COT}}$  remains challenging due to the low signal-to-noise ratio when  $D_{\text{COT}}$  is low (Lin et al., 2022). To address this issue, samples with  $D_{\text{COT}}$  less than 1.6 are filtered in the VIS+IR model, and samples with relatively large BTs at Channel-14 are filtered in the IR-single model. This filtering process significantly improves the R value from 0.869 to 0.922 in the VIS+IR model and from 0.868 to 0.911 in the IR-single model. For more details on the algorithm optimization, please refer to Appendix B.

602 or mutation (Sharma et al., 2016). In this study, continuous ground-based lidar data  
603 from the Twin Astronomy Manor in Lijiang City, Yunnan Province, China (26.454°N,  
604 100.0233°E, altitude = 3175 m) are used to evaluate the diurnal cycle characteristics  
605 of CBHs retrieved using GEO satellite algorithms (Young and Vaughan, 2009). The  
606 geographical location and photo of this station are shown in [Figure 4](#).

#### 607 [4.2.1 Comparison of CBH retrievals from ground and satellite data](#)

608 The ground-based lidar data at Lijiang station on December 6, 2018, and January  
609 8, 2019, are selected for validation. [In fact, this lidar was primarily used for the](#)  
610 [calibration of ground-based lunar radiation instruments. During the two-month](#)  
611 [observation period \(from December of 2018 to January of 2019\), it was always](#)  
612 [operated only under clear sky conditions, resulting in the capture of cloud data on just](#)  
613 [two days.](#) The number of available and [spatiotemporally](#) matched CBH sample points  
614 from ground-based lidar is 78 and 64 on December 6, 2018, and January 8, 2019,  
615 respectively. Fig 5a and 5b show the point-to-point CBH comparisons between  
616 ground-based lidar and four GEO satellite CBH algorithms on December 6, 2018, and  
617 January 8, 2019. It is worth noting that the retrieved CBHs of the two physics-based  
618 algorithms on December 6, 2018, are in good agreement with the reference values  
619 from the lidar measurements, and, in particular, the GEO CLAVR-x algorithm can  
620 obtain better results. From the results on January 8, 2019, more accurate diurnal cycle  
621 characteristics of CBHs are revealed by the GEO CLAVR-x algorithm than by the  
622 GEO IDPS algorithm.

623 Compared with the CBHs measured by ground-based lidar, the statistics of the  
624 results retrieved from the GEO IDPS algorithm are  $R = 0.67$ ,  $MAE = 3.093$  km,  $MBE$   
625 = 0.856 km, and  $RMSE = 3.609$  km (Fig. 5c). However, for cloud samples with CBH  
626 below 7.5 km, the GEO IDPS algorithm shows an obvious underestimation of CBH in  
627 [Figure 5c](#). For the GEO CLAVR-x algorithm, it can also be seen that the matched  
628 samples mostly lie near the 1:1 line with  $R = 0.773$  (the optimal CBH algorithm),  
629  $MAE = 1.319$  km,  $MBE = 0.222$  km, and  $RMSE = 1.598$  km. In addition, this figure  
630 also shows the CBH comparisons between the ML-based VIS+IR model/IR-single  
631 model algorithms and the lidar measurements, revealing that the retrieved CBH  
632 results from the ML-based VIS+IR model are better than those from the ML-based  
633 IR-single model algorithm. The comparison results between the CBHs of the  
634 ML-based VIS+IR model algorithm and the lidar measurements are around the 1:1  
635 line, with smaller errors and  $R = 0.599$ . In contrast, the  $R$  between the CBHs of the

删除了: Fig.

设置了格式: 字体: (默认) Times New Roman, (中文) DengXian, 小四, 字体颜色: 文字 1

设置了格式: 字体: (默认) Times New Roman, (中文) DengXian, 小四, 字体颜色: 文字 1

设置了格式: 字体: (默认) Times New Roman, (中文) DengXian, 小四, 字体颜色: 文字 1

删除了: spatial-temporal

删除了: Fig.

639 ML-based IR-single model algorithm and the lidar measurements is only 0.494, with a  
640 relatively large error. By comparing the retrieved CBHs with the lidar measurements  
641 at Lijiang station, it indicates that CBH results from two physics-based algorithms are  
642 remarkably more accurate, particularly that the GEO CLAVR-x algorithm can well  
643 capture diurnal variation of CBH.

644 To further assess the accuracy and quality of the diurnal cycle of CBHs retrieved  
645 with these algorithms, CBHs from another ground-based cloud radar dataset covering  
646 the entire year of 2017 are also collected and used in this study. Due to the density of  
points in the one-year time series, the point-to-point CBH comparison results for the  
entire year are not displayed here (monthly results are shown in the supplementary  
document), we only show 4 days results in the following Figure 6. As well known, the  
diurnal variation of cloud base height is primarily influenced by solar heating, causing  
the cloud base to rise in the morning and reach its peak by midday. As the surface  
cools in the afternoon and evening, the cloud base lowers, playing a crucial role in  
weather patterns and forecasting (Zheng et al., 2020). Therefore, it is essential to  
rigorously compare the ML-based algorithm with ground-based observations to  
determine its ability to adapt to the daily variations in cloud base height caused by  
natural factors. The observational instrument is a Ka-band (35 GHz) Doppler  
657 millimeter-wave cloud radar (MMCR) located at the Beijing Nanjiao Weather  
658 Observatory (a typical urban observation site) (39.81°N, 116.47°E, altitude = 32 m;  
659 see Fig. 4), performing continuous and routine observations. The MMCR provides a  
660 specific vertical resolution of 30 m and a temporal resolution of 1 minute for single  
661 profile detection, based on the radar reflectivity factor. In a previous study (Zhou et  
662 al., 2019), products retrieved by this MMCR were utilized to investigate the diurnal  
663 variations of CTH and CBH, and comparisons were made between MMCR-derived  
664 CBHs and those derived from a Vaisala CL51 ceilometer. The former study also  
665 found that the average  $R$  of CBHs from different instruments reached up to 0.65. It is  
666 worth noting that the basic physics principle for detecting cloud base height from both  
667 spaceborne cloud profiling radar and ground-based cloud radar and lidar  
668 measurements is the same. All these algorithms of detecting CBH are based on the  
669 manifest change of return signals between CBH and the clear sky atmosphere in the  
670 vertical direction (Huo et al., 2019; Ceccaldi et al., 2013). The joint spaceborne  
671 CloudSat/CALIPSO detection might face limitations in penetrating extremely dense,  
672 optically thick, or areas with heavy precipitation clouds. Hence, in comparison, the

设置了格式: 字体: (默认) Times New Roman, (中文) DengXian, 小四, 字体颜色: 文字 1

设置了格式: 字体: (默认) Times New Roman, (中文) DengXian, 小四, 字体颜色: 文字 1

设置了格式: 字体: (默认) Times New Roman, (中文) DengXian, 小四, 字体颜色: 文字 1

删除了: correlation coefficient (

删除了: )

675 CBH values gathered from ground-based lidar and cloud radar measurements are  
676 expected to be more accurate than the data derived from spaceborne  
677 CloudSat/CALIPSO detection.

678 Similar to [Figure 5](#), [Figure 6](#) presents two sample groups of CBH results from the  
679 cloud radar at Beijing Nanjiao station relative to the matched CBHs from the four  
680 retrieval algorithms (GEO IDPS, GEO CLAVR-x, ML-based IR-single, ML-based  
681 VIS+IR) on April 9–10 and July 26–28, 2017. Similar to the results at Lijiang station  
682 discussed in [Figure 5](#), we observe better and more robust performances in retrieving  
683 diurnal cycle characteristics of CBH from the two physics-based CBH retrieval  
684 algorithms. In contrast, more underestimated CBH samples are retrieved by the two  
685 ML-based algorithms.

#### 686 [4.2.2 Diurnal cycle analysis of CBH retrieval accuracy](#)

687 To further investigate the diurnal cycle characteristics of retrieved CBH from  
688 GEO satellite imager measurements, [Figure 7](#) presents box plots of the hourly CBH  
689 errors (relative to the results of cloud radar at Beijing Nanjiao station) in 2017 from  
690 the four different CBH retrieval algorithms. Remarkably, there are significant  
691 underestimations of the CBHs retrieved from the two ML-based algorithms. The  
692 ML-based VIS+IR method achieves relatively better results than the ML-based  
693 IR-single method during the daytime. Comparing the two ML-based algorithms, the  
694 errors of the IR-single model algorithm have a similar standard deviation (2.80 km) to  
695 those of the VIS+IR model algorithm (2.69 km) during the daytime. For the IR-single  
696 model algorithm, it can be applied during both daytime and nighttime, its nighttime  
697 performance degrades slightly, with an averaged RMSE (3.88 km) higher than that of  
698 daytime (3.56 km). The nighttime CBH of the IR-single model algorithm is the only  
699 choice that should be used with discretion.

700 [Figure 8](#) shows the comparisons of hourly MAE, MBE, RMSE, and R relative to  
701 the CBHs from the cloud radar at Beijing Nanjiao station during daytime between  
702 four retrieval algorithms in 2017. The RMSE of the two ML-based algorithms shows  
703 stable diurnal variation. It is noted that all algorithms have lower R at sunrise, around  
704 07:00 local time, which improve as the day progresses. However, the GEO CLAVR-x  
705 algorithm stands out for its relatively higher and more stable in R and RMSE during  
706 daytime.

707 [Figure 9a](#) displays scatter plots and relevant statistics of the CBHs retrieved from  
708 the GEO IDPS algorithm against the CBHs from cloud radar. The CBHs from the

删除了: Fig. 5, Fig. 6

删除了: Due to the density of points in the one-year time series, the point-to-point CBH comparison results for the entire year are not displayed here (monthly results are shown in the supplementary document). Similar to the results at

删除了: Fig. 5

带格式的: 缩进: 首行缩进: 0 厘米

删除了: Fig. 7

删除了: To the best of our knowledge, there is no alternative nighttime CBH product for geostationary satellite imagers right now. The nighttime CBH of the IR-single model

删除了: Fig. 8

删除了: correlation coefficients (

删除了: )

删除了: Fig.

723 GEO IDPS algorithm align well with the matched CBHs from cloud radar at Beijing  
724 Nanjiao station, with  $R = 0.515$ ,  $MAE = 2.078$  km,  $MBE = 1.168$  km, and  $RMSE =$   
725 2.669 km. In Figure 9b, the GEO CLAVR-x algorithm shows better results with  $R =$   
726 0.573,  $MAE = 2.059$  km,  $MBE = -0.204$  km, and  $RMSE = 2.601$  km. It is not  
727 surprising that Figs. 8c and 8d reveal obvious underestimated CBH results from the  
728 two ML-based CBH algorithms. Particularly, the CBH results from the ML-based  
729 VIS+IR model algorithm concentrate in the range of 2.5 km to 5 km. Therefore,  
730 Figure 5 to Figure 9 further substantiates the weak diurnal variations captured by  
731 ML-based techniques, primarily attributed to the scarcity of comprehensive CBH  
732 training samples throughout the entire day. Besides, although the two robust  
733 physics-based algorithms of GEO IDPS and GEO CLAVR-x (the optimal one) can  
734 retrieve high-quality CBHs from H8/AHI data, especially the diurnal cycle of CBH  
735 during the daytime, they still struggle to retrieve CBHs below 1 km.

## 736 5. Conclusions and discussion

737 To explore and argue the optimal and most robust CBH retrieval algorithm from  
738 geostationary satellite imager measurements, particularly focusing on capturing the  
739 typical diurnal cycle characteristics of CBH, this study employs four different  
740 retrieval algorithms (two physics-based and two ML-based algorithms). High  
741 spatiotemporal resolution CBHs are retrieved using the H8/AHI data from 2017 to  
742 2019. To assess the accuracies of the retrieved CBHs, point-to-point validations are  
743 conducted based on spatiotemporally matched CBHs from the joint  
744 CloudSat/CALIOP product, as well as ground-based lidar and cloud radar  
745 observations in China. The main findings and conclusions are outlined below.

746 Four independent CBH retrieval algorithms, namely physics-based GEO IDPS,  
747 GEO CLAVR-x, ML-based VIS+IR, and ML-based IR-single, have been developed  
748 and utilized to retrieve CBHs from GEO H8/AHI data. The two physics-based  
749 algorithms utilize cloud top and optical property products from AHI as input  
750 parameters to retrieve high spatiotemporal resolution CBHs, with operations limited  
751 to daytime. In contrast, the ML-based VIS+IR model and IR-single model algorithms  
752 use the matched joint CloudSat/CALIOP CBH product as true values for building RF  
753 prediction models. Notably, the ML-based IR-single algorithm, which relies solely on  
754 infrared band measurements, can retrieve CBH during both day and night.

763 The accuracy of CBHs retrieved from the four independent algorithms is verified  
764 using the joint CloudSat/CALIOP CBH products for the year 2017. The GEO IDPS  
765 algorithm shows an R of 0.62 and an RMSE of 2.642 km. The GEO CLAVR-x  
766 algorithm provides more accurate CBHs with an R of 0.647 and RMSE of 2.91 km.  
767 After filtering samples with optical thickness less than 1.6 and brightness temperature  
768 (at 11  $\mu$ m band) greater than 281 K, the ML-based VIS+IR and ML-based IR-single  
769 algorithms achieve higher accuracy with an R(RMSE) of 0.922(1.214 km) and  
770 0.911(1.415 km), respectively. This indicates strong agreement between the two  
771 ML-based CBH algorithms and the CloudSat/CALIOP CBH product.

772 However, in stark contrast, the results from the physics-based algorithms ([with R](#)  
773 [and RMSE of 0.592/2.86 km](#)) are superior to those from the ML-based algorithms  
774 ([with R and RMSE of 0.385/3.88 km](#)) when compared with ground-based CBH  
775 observations such as lidar and cloud radar. In the comparison with the cloud radar at  
776 Beijing Nanjiao station in 2017, the R of the GEO CLAVR-x algorithm is 0.573,  
777 while the R of the GEO IDPS algorithm is 0.515. Meanwhile, notable differences are  
778 observed in the CBHs [between](#) both ML-based algorithms. Similar conclusions are  
779 also evident in the 2-day comparisons at Yunnan Lijiang station.

780 The CBH results from the two ML-based algorithms ( $R > 0.91$ ) can likely be  
781 attributed to the use of the same training and validation dataset source as the joint  
782 CloudSat/CALIOP product. However, this dataset has limited spatial coverage and  
783 small temporal variation, potentially limiting the representativeness of the training  
784 data. In contrast, the GEO CLAVR-x algorithm demonstrates the best performance  
785 and highest accuracy in retrieving CBH from geostationary satellite data. Notably, its  
786 results align well with those from ground-based lidar and cloud radar during the  
787 daytime. However, both physics-based methods, utilizing CloudSat CPR data for  
788 regression, struggle to accurately retrieve CBHs below 1 km, as the lowest 1 km  
789 above ground level of this data is affected by ground clutter.

790 Additionally, despite utilizing the same physics principles in spaceborne and  
791 ground-based lidar/radar CBH algorithms, the previous study (Thorsen et al., 2011)  
792 has highlighted differences in profiles between them. Therefore, this factor could  
793 contribute to the relatively poorer results in CBH retrieval by ML-based algorithms  
794 compared to ground-based lidar and radar. The analysis and discussion above suggest  
795 that ML-based algorithms are constrained by the size and representativeness of their

删除了: (with R and RMSE of 0.592/2.86 km)

删除了: and

删除了: , respectively

删除了: from

800 datasets. Therefore, in scenarios involving a large time scope, such as climate  
801 research, it is more reasonable to opt for physics-based cloud base height algorithms.

802 Ideally, if more spaceborne cloud profiling radars with different passing times  
803 (covering all day) can be included in the training dataset, the promising ML technique  
804 will certainly generate a higher quality CBH product with more comprehensive  
805 observations. The CBH product using ML-based algorithms should continue to be  
806 improved in future work. Particularly, exploring the joint ML-physics-based method  
807 presents a promising direction, which can address the complexities and challenges in  
808 retrieving cloud properties. By integrating established physical relationships into ML  
809 models, we can potentially enhance the accuracy and reliability of predictions. This  
810 approach not only leverages the strengths of both physics-based models and  
811 data-driven techniques but also offers a pathway to more robust and interpretable  
812 solutions in atmospheric sciences. At present, we will focus on developing  
813 physics-based algorithms for cloud base height for the next generation of  
814 geostationary meteorological satellites, to support the application of these products in  
815 weather and climate domains.

816 Besides, at night, current GEO satellite imaging instruments encounter  
817 challenges in accurately determining CBH due to limited or absent solar illumination.  
818 Because it is unable to retrieve cloud optical depth in the visible band, the current  
819 method faces limitations. However, there is potential for enhanced accuracy in  
820 deriving cloud optical and microphysical properties, as well as CBH, by incorporating  
821 the Day/Night Band (DNB) observations during nighttime in the future (Walther et al.,  
822 2013).

823

824

825 *Data availability.* The authors would like to acknowledge NASA, JMA, Colorado  
826 State University, and NOAA for freely providing the MODIS  
827 (<https://ladsweb.modaps.eosdis.nasa.gov/search>), CloudSat/CALIOP  
828 (<https://www.cloudsat.cira.colostate.edu/>), Himawari-8 (<ftp://ptree.jaxa.jp>), and GFS  
829 NWP (<ftp://nomads.ncdc.noaa.gov/GFS/Grid4>) data online, respectively.

830

831

832 *Author contributions.* MM proposed the essential research idea. MW, MM, JL, HL,

删除了: ↵

删除了: University of Colorado

835 BC, and YL performed the analysis and drafted the manuscript. ZY and NX provided  
836 useful comments. All the authors contributed to the interpretation and discussion of  
837 results and the revision of the manuscript.

838

839

840 *Competing interests.* The authors declare that they have no conflict of interest.

841

842

843 *Acknowledgements.* The authors would like to acknowledge NASA, JMA, University  
844 of Colorado, and NOAA for freely providing satellite data online, respectively. The  
845 authors thank NOAA, NASA, and their VIIRS algorithm working groups (AWG) for  
846 freely providing the VIIRS cloud base height algorithm theoretical basic  
847 documentations (ATBD). In addition, the authors appreciate the power computer tools  
848 developed by the Python and scikit-learn groups (<http://scikit-learn.org>). Besides the  
849 authors also thank Rundong Zhou and Pan Xia for drawing some pictures of this  
850 manuscript. Last but not the least, the authors sincerely thank Prof. Yong Zhang and  
851 Prof. Jianping Guo for freely providing cloud base height results retrieved by  
852 ground-based cloud radar at Beijing Nanjiao station. This work was supported partly  
853 by the Guangdong Major Project of Basic and Applied Basic Research (Grant  
854 2020B0301030004), National Natural Science Foundation of China under Grants  
855 42175086 and U2142201, FengYun Meteorological Satellite Innovation Foundation  
856 under Grant FY-APP-ZX-2022.0207, the Innovation Group Project of Southern  
857 Marine Science and Engineering Guangdong Laboratory (Zhuhai) (No.  
858 SML2023SP208), and the Science and Technology Planning Project of Guangdong  
859 Province (2023B1212060019). We would like to thank the editor and anonymous  
860 reviewers for their thoughtful suggestions and comments.

861

862

## 863 **Appendix A**

864 Based on the previously discussed description of two physics-based cloud base

删除了: the Natural Science Foundation of Shanghai (No. 21ZR1419800), the Guangdong Major Project of Basic and

删除了: Innovation Group Project of Southern Marine Science and Engineering Guangdong Laboratory (Zhuhai) (No. 311022006),

870 height (CBH) retrieval algorithms (GEO IDPS and GEO CLAVR-x retrieval  
871 algorithms), cloud products such as cloud top height (CTH), effective particle radius  
872 ( $R_{\text{eff}}$ ), and cloud optical thickness ( $D_{\text{COT}}$ ) will be utilized in both algorithms. To  
873 validate the reliability of these cloud products derived from the Advanced Himawari  
874 Imager (AHI) aboard the Himawari-8 (H8), a pixel-by-pixel comparison is conducted  
875 with analogous MODIS Collection-6.1 Level-2 cloud products. Both Aqua and Terra  
876 MODIS Level-2 cloud products (MOD06 and MYD06) are accessible for free  
877 download from the MODIS official website. For verification purposes, the  
878 corresponding Level-2 cloud products from January, April, July, and October of 2018  
879 are chosen to assess CTH,  $D_{\text{COT}}$ , and  $R_{\text{eff}}$  retrieved by H8/AHI.

880 [Figure S2](#) (in the supplementary document) shows the spatiotemporally matched  
881 case comparisons of CTH,  $D_{\text{COT}}$  and  $R_{\text{eff}}$  from H8/AHI and Terra/MODIS (MYD06)  
882 at 03:30 UTC on January 15, 2018. It can be seen that the CTH,  $D_{\text{COT}}$  and  $R_{\text{eff}}$  from  
883 H8/AHI are in good agreement with the matched MODIS cloud products. However,  
884 there are still some differences in  $R_{\text{eff}}$  at the regions near 35°N, 110°E in [Figures S2d](#)  
885 and S2c. The underestimated  $R_{\text{eff}}$  values from H8/AHI relative to MODIS have been  
886 reported in previous studies. (Letu et al., 2019) compared the ice cloud products  
887 retrieved from AHI and MODIS, and concluded that the  $R_{\text{eff}}$  from both products differ  
888 remarkably in the ice cloud region and the  $D_{\text{COT}}$  from them are roughly similar.  
889 However, the  $D_{\text{COT}}$  from AHI data is higher in some areas. Looking again at the cloud  
890 optical thickness that at the same time, the slight underestimation of H8/AHI  $D_{\text{COT}}$   
891 can be found in [Figures S2e](#) and S2f. [Figure S3](#) (in the supplementary document)  
892 shows another case at 02:10 UTC on January 15, 2018. Despite of the good  
893 consistence between H8/AHI and MODIS cloud products, there are slight differences  
894 in CTH in the area around 40°S–40.5°S, 100°E–110°E in Figs. S3a and S3b. Besides,  
895 as shown in [Figure S2](#), there are still underestimations in the  $R_{\text{eff}}$  of H8/AHI.

896 To further compare and validate these three H8/AHI cloud products, the  
897 spatiotemporally matched samples from H8/AHI and Aqua/Terra MODIS in four  
898 months of 2018 are counted within the three intervals of 0.1 km (CTH), 1.0  $\mu\text{m}$  ( $R_{\text{eff}}$ ),  
899 and 1 ( $D_{\text{COT}}$ ) in [Figure S4](#) (in the supplementary document). The corresponding mean  
900 absolute error, mean bias error, [RMSE](#) and  $R$  values are also calculated and marked in  
901 each subfigure. As can be seen, the  $R$  of CTH is around 0.75 in all four months and is  
902 close to 0.8 in August. The results of  $D_{\text{COT}}$  show the highest  $R$ , reaching above 0.8. In  
903 contrast, the underestimation trend in  $R_{\text{eff}}$  is also shown in this figure. These different

删除了:..

删除了: spatially-temporal

删除了:..

删除了:..

删除了:..

删除了:..

删除了: spatially-temporally

删除了:..

删除了: root mean square error

删除了: correlation coefficient (

删除了:)

915 consistencies between two satellite-retrieved cloud products may be attributed to: (1)  
916 different spatiotemporal resolutions between H8/AHI and MODIS; (2) different  
917 wavelength bands, bulk scattering model, and specific algorithm used for retrieving  
918 cloud products; (3) different view zenith angle between GEO and low-earth-orbit  
919 satellite platforms (Letu et al., 2019). In addition, other external factors such as  
920 surface type also can affect the retrieval of cloud product. However, according to  
921 Figure S4, the bulk of the analyzed samples are still around the 1:1 line, indicating the  
922 good quality of H8/AHI cloud products.

删除了: spatial-temporal

923

## 924 Appendix B

925 The ML-based visible (VIS)+infrared (IR) model algorithm mentioned above  
926 uses 230 typical variables (see Table 1) as model predictors, and the importance  
927 scores of top-30 predictors are ranked in Figure S5 (in the supplementary document).  
928 It can be seen that the most important variables are CTH and CTT, and Dcot is an  
929 important or sensitive factor affecting these two quantities. A sensitivity test is also  
930 performed to further investigate the potential influence of Dcot on the CBH retrieval  
931 by the VIS+IR model (see Table S1 in the supplementary document). From Figure  
932 S7a, we find that the samples with Dcot lower than 5 cause the relatively large CBH  
933 errors compared with the matched CBHs from the joint CALIPSO (Cloud-Aerosol  
934 Lidar and Infrared Pathfinder Satellite Observation)/CloudSat product.

935 According to the results in this Figure S7b, we may filter the samples with  
936 relatively small Dcot to further improve the accuracy of CBH retrieval by the VIS+IR  
937 model (see Table S1). Figure S7b shows that after filtering the samples with the Dcot  
938 less than 1.6, the R increases from 0.895 to 0.922, implying a better performance of  
939 CBH retrieval. According to the ranking of predictor importance (see Fig. S6 in the  
940 supplementary document), we also conduct another sensitivity test on the BT  
941 observed by H8/AHI IR Channel-14 (Cha14) at 11  $\mu$ m, which plays an important role  
942 in the IR-single model. Figure S7c shows that the BT values of H8/AHI Channel-14  
943 ranges from 160 K to 316 K, and the samples with BT higher than 300 K show large  
944 CBH errors. Similarly, by filtering the samples with BT higher than 281 K, we can get  
945 a better IR-single model algorithm for retrieving high-quality CBH (see Table S2 in  
946 the supplementary document). Figure S7d also proves that the R value increases from  
947 0.868 to 0.911.

948

删除了: ..

删除了: cloud top temperature

删除了: ..

删除了: ..

删除了: ..

删除了: B3

删除了: ..

删除了: ..

959 **Reference**

960 Aydin, K. and Singh, J.: Cloud Ice Crystal Classification Using a 95-GHz Polarimetric Radar, *Journal of*  
961 *Atmospheric and Oceanic Technology*, 21, 1679–1688, <https://doi.org/10.1175/JTECH1671.1>, 2004.

962 Baker, N.: Joint Polar Satellite System (JPSS) VIIRS Cloud Base Height Algorithm Theoretical Basis  
963 Document (ATBD), 2011.

964 Baum, B., Menzel, W. P., Frey, R., Tobin, D., Holz, R., and Ackerman, S.: MODIS cloud top property  
965 refinements for Collection 6, *Journal of Applied Meteorology and Climatology*, 51, 1145-1163,  
966 10.1175/JAMC-D-11-0203.1, 2012.

967 Bessho, K., Date, K., Hayashi, M., Ikeda, A., Imai, T., Inoue, H., Kumagai, Y., Miyakawa, T., Murata, H.,  
968 Ohno, T., Okuyama, A., Oyama, R., Sasaki, Y., Shimazu, Y., Shimoji, K., Sumida, Y., Suzuki, M., Taniguchi,  
969 H., Tsuchiyama, H., Uesawa, D., Yokota, H., and Yoshida, R.: An introduction to Himawari-8/9—Japan's  
970 new-generation geostationary meteorological satellites, *Journal of the Meteorological Society of*  
971 *Japan*, 94, 151-183, 10.2151/jmsj.2016-009, 2016.

972 Breiman, L.: Random forests, *Machine Learning*, 45, 5-32, 2001.

973 Ceccaldi, M., Delanoë, J., Hogan, R. J., Pounder, N. L., Protat, A., and Pelon, J.: From CloudSat-CALIPSO  
974 to EarthCare: Evolution of the DARDAR cloud classification and its comparison to airborne radar-lidar  
975 observations, *Journal of Geophysical Research: Atmospheres*, 118, 7962-7981, 10.1002/jgrd.50579,  
976 2013.

977 Forsythe, J. M., Haar, T. H. V., and Reinke, D. L.: Cloud-Base height estimates using a combination of  
978 Meteorological Satellite Imagery and Surface Reports, *Journal of Applied Meteorology and Climatology*,  
979 39, 2336–2347, [https://doi.org/10.1175/1520-0450\(2000\)039<2336:CBHEUA>2.0.CO;2](https://doi.org/10.1175/1520-0450(2000)039<2336:CBHEUA>2.0.CO;2), 2000.

980 Gregorutti, B., Michel, B., and Saint-Pierre, P.: Correlation and variable importance in random forests,  
981 *Statistics and Computing*, 27, 659-678, 10.1007/s11222-016-9646-1, 2017.

982 Håkansson, N., Adok, C., Thoss, A., Scheirer, R., and Hörnquist, S.: Neural network cloud top pressure  
983 and height for MODIS, *Atmospheric Measurement Techniques*, 11, 3177–3196,  
984 10.5194/amt-11-3177-2018, 2018.

985 Hansen, B.: A Fuzzy Logic-Based Analog Forecasting System for Ceiling and Visibility, *Weather and*  
986 *Forecasting*, 22, 1319-1330, 10.1175/2007waf2006017.1, 2007.

987 Hartmann, D. L. and Larson, K.: An important constraint on tropical cloud - climate feedback, *Geophys*  
988 *Res Lett*, 29, 12-11-12-14, 10.1029/2002gl015835, 2002.

989 Heidinger, A. and Pavolonis, M.: Gazing at cirrus clouds for 25 years through a split window, part 1:  
990 Methodology, *Journal of Applied Meteorology and Climatology*, 48, 1110-1116,  
991 10.1175/2008JAMC1882.1, 2009.

992 Heidinger, A. K., Bearson, N., Foster, M. J., Li, Y., Wanzong, S., Ackerman, S., Holz, R. E., Platnick, S., and  
993 Meyer, K.: Using sounder data to improve cirrus cloud height estimation from satellite imagers,  
994 *Journal of Atmospheric and Oceanic Technology*, 36, 1331-1342, 10.1175/jtech-d-18-0079.1, 2019.

995 Heymsfield, A. J., Bansemer, A., Matrosov, S., and Tian, L.: The 94-GHz radar dim band: Relevance to  
996 ice cloud properties and CloudSat, *Geophys. Res. Lett.*, 35, 10.1029/2007GL031361, 2008.

997 Hirsch, E., Agassi, E., and Koren, I.: A novel technique for extracting clouds base height using ground  
998 based imaging, *Atmospheric Measurement Techniques*, 4, 117-130, 10.5194/amt-4-117-2011, 2011.

999 Hunt, W. H., Winker, D. M., Vaughan, M. A., Powell, K. A., Lucker, P. L., and Weimer, C.: CALIPSO lidar  
1000 description and performance assessment, *J. Atmos. Oceanic. Technol.*, 26, 2009.

1001 Huo, J., Bi, Y., Lü, D., and Duan, S.: Cloud Classification and Distribution of Cloud Types in Beijing Using  
1002 Ka-Band Radar Data, *Advances in Atmospheric Sciences*, 36, 793-803, 10.1007/s00376-019-8272-1,

1003 2019.

1004 Hutchison, K., Wong, E., and Ou, S. C.: Cloud base heights retrieved during night-time conditions with  
1005 MODIS data, *Int J Remote Sens*, 27, 2847-2862, 10.1080/01431160500296800, 2006.

1006 Hutchison, K. D.: The retrieval of cloud base heights from MODIS and three-dimensional cloud fields  
1007 from NASA's EOS Aqua mission, *Int J Remote Sens*, 23, 5249-5265, 10.1080/01431160110117391,  
1008 2002.

1009 Iwabuchi, H., Putri, N. S., Saito, M., Tokoro, Y., Sekiguchi, M., Yang, P., and Baum, B. A.: Cloud Property  
1010 Retrieval from Multiband Infrared Measurements by Himawari-8, *Journal of the Meteorological  
1011 Society of Japan. Ser. II*, 96B, 27-42, 10.2151/jmsj.2018-001, 2018.

1012 Kalnay, E., Kanamitsu, M., Kistler, R., Collins, W., Deaven, D., Gandin, L., Iredell, M., Saha, S., White, G.,  
1013 Woollen, J., Zhu, Y., Leetmaa, A., Reynolds, R., Chelliah, M., Ebisuzaki, W., Higgins, J., Mo,  
1014 K. C., Ropelewski, C., and Wang, J.: The NCEP NCAR 40-Year Reanalysis Project, 1996.

1015 Kühnlein, M., Appelhans, T., Thies, B., and Nauß, T.: Precipitation Estimates from MSG SEVIRI Daytime,  
1016 Nighttime, and Twilight Data with Random Forests, *Journal of Applied Meteorology and Climatology*,  
1017 53, 2457-2480, 10.1175/jamc-d-14-0082.1, 2014.

1018 Letu, H., Nagao, T. M., Nakajima, T. Y., Riedi, J., Ishimoto, H., Baran, A. J., Shang, H., Sekiguchi, M., and  
1019 Kikuchi, M.: Ice cloud properties from Himawari-8/AHI next-generation geostationary satellite:  
1020 Capability of the AHI to monitor the DC cloud generation process, *IEEE Transactions on Geoscience  
1021 and Remote Sensing*, 57, 3229-3239, 10.1109/tgrs.2018.2882803, 2019.

1022 Li, Y., Yi, B., and Min, M.: Diurnal variations of cloud optical properties during day-time over China  
1023 based on Himawari-8 satellite retrievals, *Atmospheric Environment*, 277, 119065,  
1024 10.1016/j.atmosenv.2022.119065, 2022.

1025 Liang, Y., Min, M., Yu, Y., Wang, X., and Xia, P.: Assessing diurnal cycle of cloud covers of Fengyun-4A  
1026 geostationary satellite based on the manual observation data in China, *IEEE Transactions on  
1027 Geoscience and Remote Sensing*, 61, 10.1109/TGRS.2023.3256365, 2023.

1028 Lin, H., Li, Z., Li, J., Zhang, F., Min, M., and Menzel, W. P.: Estimate of daytime single-layer cloud base  
1029 height from Advanced Baseline Imager measurements, *Remote Sensing of Environment*, 274, 112970,  
1030 10.1016/j.rse.2022.112970, 2022.

1031 Lu, X., Mao, F., Rosenfeld, D., Zhu, Y., Pan, Z., and Gong, W.: Satellite retrieval of cloud base height and  
1032 geometric thickness of low-level cloud based on CALIPSO, *Atmospheric Chemistry and Physics*, 21,  
1033 10.5194/acp-21-11979-2021, 2021.

1034 Meerkötter, R. and Bugliaro, L.: Diurnal evolution of cloud base heights in convective cloud fields from  
1035 MSG/SEVIRI data *Atmospheric Chemistry and Physics*, 9, 1767-1778, 10.5194/acp-9-1767-2009,  
1036 2009.

1037 Miller, R. M., Rauber, R. M., Girolamo, L. D., Rilloraza, M., Fu, D., McFarquhar, G. M., Nesbitt, S. W.,  
1038 Ziembka, L. D., Woods, S., and Thornhill, K. L.: Influence of natural and anthropogenic aerosols on cloud  
1039 base droplet size distributions in clouds over the South China Sea and West Pacific, *Atmospheric  
1040 Chemistry and Physics*, 23, 8959-8977, 10.5194/acp-23-8959-2023, 2023.

1041 Miller, S. D., Rogers, M. A., Haynes, J. M., Sengupta, M., and Heidinger, A. K.: Short-term solar  
1042 irradiance forecasting via satellite/model coupling, *Solar Energy*, 168, 102-117,  
1043 10.1016/j.solener.2017.11.049, 2018.

1044 Min, M. and Zhang, Z.: On the influence of cloud fraction diurnal cycle and sub-grid cloud optical  
1045 thickness variability on all-sky direct aerosol radiative forcing, *Journal of Quantitative Spectroscopy  
1046 and Radiative Transfer*, 142, 25-36, 10.1016/j.jqsrt.2014.03.014, 2014.

1047 Min, M., Li, J., Wang, F., Liu, Z., and Menzel, W. P.: Retrieval of cloud top properties from advanced  
1048 geostationary satellite imager measurements based on machine learning algorithms, *Remote Sensing*  
1049 of Environment

1050 Min, M., Chen, B., Xu, N., He, X., Wei, X., and Wang, M.: Nonnegligible diurnal and long-term variation  
1051 characteristics of the calibration biases in Fengyun-4A/AGRI infrared channels based on the oceanic  
1052 drifter data, *IEEE Transactions on Geoscience and Remote Sensing*, 60, 1-15,  
1053 10.1109/TGRS.2022.3160450, 2022.

1054 Min, M., Wu, C., Li, C., Liu, H., Xu, N., Wu, X., Chen, L., Wang, F., Sun, F., Qin, D., Wang, X., Li, B., Zheng,  
1055 Z., Cao, G., and Dong, L.: Developing the science product algorithm testbed for Chinese  
1056 next-generation geostationary meteorological satellites: FengYun-4 series, *Journal of Meteorological*  
1057 *Research*, 31, 708-719, 10.1007/s13351-017-6161-z, 2017.

1058 Noh, Y.-J., Miller, S. D., Seaman, C. J., Haynes, J. M., Li, Y., Heidinger, A. K., and Kulie, M. S.: Enterprise  
1059 AWG Cloud Base Algorithm (ACBA), 2022.

1060 Noh, Y.-J., Forsythe, J. M., Miller, S. D., Seaman, C. J., Li, Y., Heidinger, A. K., Lindsey, D. T., Rogers, M. A.,  
1061 and Partain, P. T.: Cloud-base height estimation from VIIRS. Part II: A statistical algorithm based on  
1062 A-Train satellite data, *Journal of Atmospheric and Oceanic Technology*, 34, 585-598,  
1063 10.1175/JTECH-D-16-0110.1, 2017.

1064 Omar, A., Winker, D., Kittaka, C., Vaughan, M., Liu, Z., Hu, Y., Trepte, C., Rogers, R., Ferrare, R., Kuehn,  
1065 R., and Hostetler, C.: The CALIPSO automated aerosol classification and lidar ratio selection algorithm,  
1066 *J. Atmos. Oceanic. Technol.*, 26, 1994-2014, 10.1175/2009JTECHA1231, 2009.

1067 Platnick, S., Meyer, K. G., King, M. D., Wind, G., Amarasinghe, N., Marchant, B., Arnold, G. T., Zhang, Z.,  
1068 Hubanks, P. A., Holz, R. E., Yang, P., Ridgway, W. L., and Riedi, J.: The MODIS cloud optical and  
1069 microphysical products: Collection 6 updates and examples from Terra and Aqua, *IEEE Trans Geosci*  
1070 *Remote Sens*, 55, 502-525, 10.1109/TGRS.2016.2610522, 2017.

1071 Rosenfeld, D., Zheng, Y., Hashimshoni, E., Pohlker, M. L., Jefferson, A., Pohlker, C., Yu, X., Zhu, Y., Liu, G.,  
1072 Yue, Z., Fischman, B., Li, Z., Giguzin, D., Goren, T., Artaxo, P., Barbosa, H. M., Poschl, U., and Andreae,  
1073 M. O.: Satellite retrieval of cloud condensation nuclei concentrations by using clouds as CCN chambers,  
1074 *Proc. Natl. Acad. Sci.*, 113, 5828-5834, 10.1073/pnas.1514044113, 2016.

1075 Sassen, K. and Wang, Z.: Classifying clouds around the globe with the CloudSat radar: 1-year of results,  
1076 *Geophys. Res. Lett.*, 35, 1-5, doi:10.1029/2007GL032591, 2008.

1077 Seaman, C. J., Noh, Y.-J., Miller, S. D., Heidinger, A. K., and Lindsey, D. T.: Cloud-base height estimation  
1078 from VIIRS. Part I: Operational algorithm validation against CloudSat, *Journal of Atmospheric and*  
1079 *Oceanic Technology*, 34, 567-583, 10.1175/jtech-d-16-0109.1, 2017.

1080 Sharma, S., Vaishnav, R., Shukla, M. V., Kumar, P., Kumar, P., Thapliyal, P. K., Lal, S., and Acharya, Y. B.:  
1081 Evaluation of cloud base height measurements from Ceilometer CL31 and MODIS satellite over  
1082 Ahmedabad, India, *Atmospheric Measurement Techniques*, 9, 711-719, 10.5194/amt-9-711-2016,  
1083 2016.

1084 Stephens, G. L., Vane, D. G., Boain, R. J., Mace, G. G., and Sassen, K.: The CloudSat mission and the  
1085 A-Train: A new dimension of space-based observations of clouds and precipitation, *Bull. Amer. Meteor.*  
1086 *Soc.*, 83, 1771-1790, 2002.

1087 Stubenrauch, C. J., Rossow, W. B., Kinne, S., Ackerman, S., Cesana, G., Chepfer, H., Di Girolamo, L.,  
1088 Getzewich, B., Guignard, A., Heidinger, A., Maddux, B. C., Menzel, W. P., Minnis, P., Pearl, C., Platnick,  
1089 S., Poulsen, C., Riedi, J., Sun-Mack, S., Walther, A., Winker, D., Zeng, S., and Zhao, G.: Assessment of  
1090 global cloud datasets from satellites: project and database initiated by the GEWEX radiation panel,

1091 Bulletin of the American Meteorological Society, 94, 1031-1049, 10.1175/bams-d-12-00117.1, 2013.

1092 Su, T., Zheng, Y., and Li, Z.: Methodology to determine the coupling of continental clouds with surface  
1093 and boundary layer height under cloudy conditions from lidar and meteorological data, Atmospheric  
1094 Chemistry and Physics, 22, 1453-1466, 10.5194/acp-22-1453-2022, 2022.

1095 Tan, Z., Huo, J., Ma, S., Han, D., Wang, X., Hu, S., and Yan, W.: Estimating cloud base height from  
1096 Himawari-8 based on a random forest algorithm, Int J Remote Sens, 42, 2485-2501,  
1097 10.1080/01431161.2020.1854891, 2020.

1098 Thorsen, T. J., Fu, Q., and Comstock, J.: Comparison of the CALIPSO satellite and ground-based  
1099 observations of cirrus clouds at the ARM TWP sites, Journal of Geophysical Research: Atmospheres,  
1100 116, 10.1029/2011jd015970, 2011.

1101 Viúdez-Mora, A., Costa-Surós, M., Calbó, J., and González, J. A.: Modeling atmospheric longwave  
1102 radiation at the surface during overcast skies: The role of cloud base height, Journal of Geophysical  
1103 Research: Atmospheres, 120, 199-214, 10.1002/2014jd022310, 2015.

1104 Wang, F., Min, M., Xu, N., Liu, C., Wang, Z., and Zhu, L.: Effects of linear calibration errors at low  
1105 temperature end of thermal infrared band: Lesson from failures in cloud top property retrieval of  
1106 FengYun-4A geostationary satellite, IEEE Transactions on Geoscience and Remote Sensing, 60,  
1107 5001511, 10.1109/TGRS.2022.3140348, 2022.

1108 Wang, T., Shi, J., Ma, Y., Letu, H., and Li, X.: All-sky longwave downward radiation from satellite  
1109 measurements: General parameterizations based on LST, column water vapor and cloud top  
1110 temperature, ISPRS Journal of Photogrammetry and Remote Sensing, 161, 52-60,  
1111 10.1016/j.isprsjprs.2020.01.011, 2020.

1112 Wang, X., Min, M., Wang, F., Guo, J., Li, B., and Tang, S.: Intercomparisons of cloud mask product  
1113 among Fengyun-4A, Himawari-8 and MODIS, IEEE Transactions on Geoscience and Remote Sensing, 57,  
1114 8827-8839, 10.1109/TGRS.2019.2923247 2019.

1115 Wang, Z., Vane, D., Stephens, G., Reinke, D., and TBD: Level 2 combined radar and lidar cloud scenario  
1116 classification product process description and interface control document, 2012.

1117 Warren, S. G. and Eastman, R.: Diurnal Cycles of Cumulus, Cumulonimbus, Stratus, Stratocumulus, and  
1118 Fog from Surface Observations over Land and Ocean, J Climate, 27, 2386-2404,  
1119 10.1175/jcli-d-13-00352.1, 2014.

1120 Winker, D. M., Vaughan, M. A., Omar, A., Hu, Y., Powell, K. A., Liu, Z., Hunt, W. H., and Young, S. A.:  
1121 Overview of the CALIPSO mission and CALIOP data processing algorithms, J. Atmos. Oceanic Technol.,  
1122 26, 2310-2323, 10.1175/2009JTECHA1281.1, 2009.

1123 Yang, J., Li, S., Gong, W., Min, Q., Mao, F., and Pan, Z.: A fast cloud geometrical thickness retrieval  
1124 algorithm for single-layer marine liquid clouds using OCO-2 oxygen A-band measurements, Remote  
1125 Sensing of Environment, 256, 10.1016/j.rse.2021.112305, 2021.

1126 Young, S. A. and Vaughan, M. A.: The retrieval of profiles of particulate extinction from Cloud Aerosol  
1127 Lidar Infrared Pathfinder Satellite Observations (CALIPSO) data: Algorithm description, J. Atmos.  
1128 Oceanic. Technol., 26, 1105-1119, 10.1175/2008JTECHA1221.1, 2009.

1129 Zhang, Y., Zhang, L., Guo, J., Feng, J., Cao, L., Wang, Y., Zhou, Q., Li, L., Li, B., Xu, H., Liu, L., An, N., and  
1130 Liu, H.: Climatology of cloud-base height from long-term radiosonde measurements in China,  
1131 Advances in Atmospheric Sciences, 35, 158-168, 10.1007/s00376-017-7096-0, 2018.

1132 Zheng, Y. and Rosenfeld, D.: Linear relation between convective cloud base height and updrafts and  
1133 application to satellite retrievals, Geophys Res Lett, 42, 6485-6491, 10.1002/2015gl064809, 2015.

1134 Zheng, Y., Sakradzija, M., Lee, S.-S., and Li, Z.: Theoretical Understanding of the Linear Relationship

1135 between Convective Updrafts and Cloud-Base Height for Shallow Cumulus Clouds. Part II: Continental  
1136 Conditions, *J Atmos Sci*, 77, 1313-1328, 10.1175/jas-d-19-0301.1, 2020.  
1137 Zhou, Q., Zhang, Y., Li, B., Li, L., Feng, J., Jia, S., Lv, S., Tao, F., and Guo, J.: Cloud-base and cloud-top  
1138 heights determined from a ground-based cloud radar in Beijing, China, *Atmospheric Environment*, 201,  
1139 381-390, 10.1016/j.atmosenv.2019.01.012, 2019.  
1140 Zhou, R., Pan, X., Xiaohu, Z., Na, X., and Min, M.: Research progress and prospects of atmospheric  
1141 motion vector based on meteorological satelliteimages, *Reviews of Geophysics and Planetary Physics*  
1142 (In Chinese), 55, 184-194, 10.19975/j.dqyx.2022-077, 2024.  
1143 Zhu, Y., Rosenfeld, D., Yu, X., Liu, G., Dai, J., and Xu, X.: Satellite retrieval of convective cloud base  
1144 temperature based on the NPP/VIIRS Imager, *Geophys Res Lett*, 41, 1308-1313,  
1145 10.1002/2013gl058970, 2014.  
1146  
1147  
1148  
1149  
1150  
1151  
1152  
1153  
1154  
1155  
1156  
1157  
1158  
1159  
1160  
1161  
1162  
1163  
1164  
1165  
1166  
1167  
1168  
1169  
1170

1171

1172 **Tables and Figures**

1173

1174 **Table 1.** Predictand and predictor variables for both visible (VIS)+infrared (IR) model  
1175 and IR-single regression model training, which are divided according to the different  
1176 predictor variables from satellite and NWP data

<u>Predictand</u>	<u>IR-single model input</u>	<u>VIS+IR model input</u>
<u>Predictor</u>	<u>BT(3.9<math>\mu</math>m), BT(6.2<math>\mu</math>m), BT(6.9<math>\mu</math>m), BT(7.3<math>\mu</math>m), BT(8.6<math>\mu</math>m), BT(9.6<math>\mu</math>m), BT(10.4<math>\mu</math>m), BT(11.2<math>\mu</math>m), BT(12.4<math>\mu</math>m), BT(13.3<math>\mu</math>m), BTD(11.2–12.4<math>\mu</math>m), BTD(11.2– 13.3<math>\mu</math>m) [Unit = K], Air Mass (1/cos(VZA)), View azimuth angles [Unit = degree],</u>	<u>BT(3.9<math>\mu</math>m), BT(6.2<math>\mu</math>m), BT(6.9<math>\mu</math>m), BT(7.3<math>\mu</math>m), BT(8.6<math>\mu</math>m), BT(9.6<math>\mu</math>m), BT(10.4<math>\mu</math>m), BT(11.2<math>\mu</math>m), BT(12.4<math>\mu</math>m), BT(13.3<math>\mu</math>m), BTD(11.2–12.4<math>\mu</math>m), BTD(11.2– 13.3<math>\mu</math>m) [Unit = K], Air Mass(1/cos(VZA)), Air Mass(1/cos(SZA)),</u>
<u>[satellite measurements]</u>	<u>Cloud top height from H8/AHI [unit: m], Cloud top temperature from H8/AHI [unit: K]</u>	<u>View/Solar Azimuth angles [Unit = degree], Cloud top height from H8/AHI [unit: m], Cloud top temperature from H8/AHI [unit: K] Ref(0.47<math>\mu</math>m), Ref(0.51<math>\mu</math>m), Ref(0.64<math>\mu</math>m), Ref(0.86<math>\mu</math>m), Ref(1.64<math>\mu</math>m), Ref(2.25<math>\mu</math>m)</u>
<u>Predictor  GFS NWP </u>	<u>Altitude profile (from surface to about 21 km, 67 layers) [unit: m], Temperature profile (from surface to about 21 km, 67 layers) [unit: K], Relative humidity profile (from surface to about 21 km, 67 layers) [unit: %], Total precipitable water, Surface temperature [unit: K]</u>	<u>Altitude profile (from surface to about 21 km, 67 layers) [unit: m], Temperature profile (from surface to about 21 km, 67 layers) [unit: K], Relative humidity profile (from surface to about 21 km, 67 layers) [unit: %], Total precipitable water, Surface temperature [unit: K]</u>
<u>Predictor [other]</u>	<u>Surface elevation [unit: m]</u>	<u>Surface elevation [unit: m]</u>

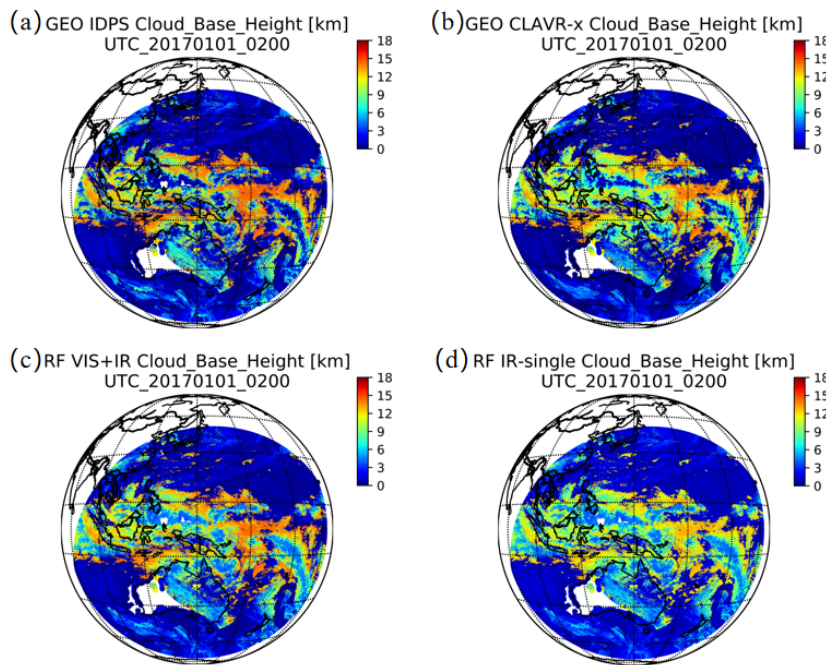
1177 Notes: VZA = view zenith angle [unit: degree]; SZA = solar zenith angle [unit:  
1178 degree]

1179

1180

1181

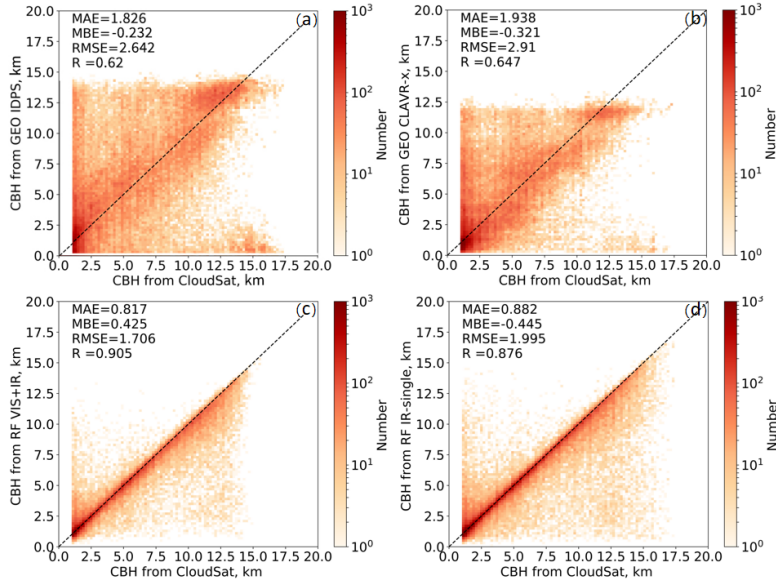
1182  
1183  
1184  
1185  
1186  
1187  
1188  
1189  
1190  
1191



1192  
1193 **Figure 1.** Comparison of full disk CBH results retrieved by the four-independent  
1194 algorithms at 02:00 UTC on January 1, 2017. (a) GEO IDPS algorithm, (b) GEO  
1195 Clouds from AVHRR Extended (CLAVR-x) algorithm, (c) ML-based (RF, random  
1196 forest) VIS+IR algorithm and (d) ML-based (RF) IR-single algorithm.

1197  
1198  
1199  
1200  
1201  
1202  
1203

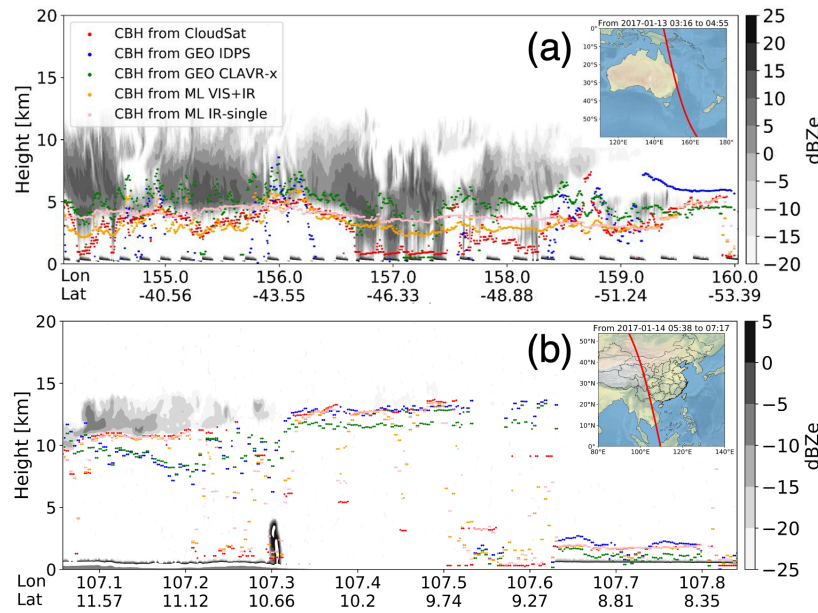
1204  
1205  
1206  
1207



1208  
1209 **Figure 2.** Density distributions of CBHs retrieved from (a) GEO  
1210 CLAVR-x, (b) VIS+IR and (d) IR-single algorithms compared with the CBHs from  
1211 the joint CloudSat/CALIPSO product (taken as true values) in 2017. The mean  
1212 absolute error (MAE), mean bias error (MBE), root mean square error (RMSE) and R  
1213 are listed in each subfigure where the difference exceeds the 95% significance level ( $p$   
1214  $< 0.05$ ) according to the Pearson's  $\chi^2$  test.

1215  
1216  
1217  
1218  
1219  
1220  
1221  
1222  
1223

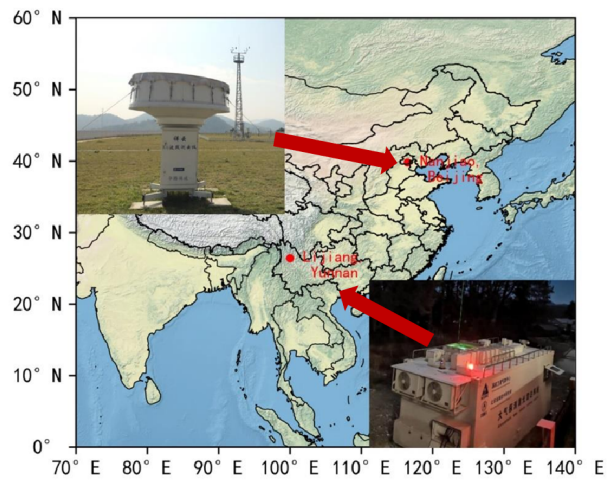
1224  
1225  
1226  
1227



1229 **Figure 3.** Inter-comparisons of CBH products retrieved by CloudSat (red solid circle),  
1230 the GEO IDPS algorithm (blue solid circle), the GEO CLAVR-x (green solid circle),  
1231 the ML-based VIS+IR model algorithm (orange solid circle), and the ML-based  
1232 IR-single model algorithm (pink solid circle) at (a) 03:16–04:55 UTC on January 13,  
1233 2017 (a) and (b) 05:38–07:17 UTC on January 14, 2017. The black and gray colormap  
1234 represents the matched CloudSat radar reflectivity.

1235  
1236  
1237  
1238  
1239  
1240  
1241  
1242

1243  
1244  
1245  
1246  
1247



1248

1249 **Figure 4.** Geographical locations and photos of lidar and cloud radar at Yunnan  
1250 Lijiang and Beijing Nanjiao stations.

1251  
1252  
1253  
1254  
1255  
1256  
1257  
1258  
1259  
1260  
1261  
1262  
1263  
1264  
1265

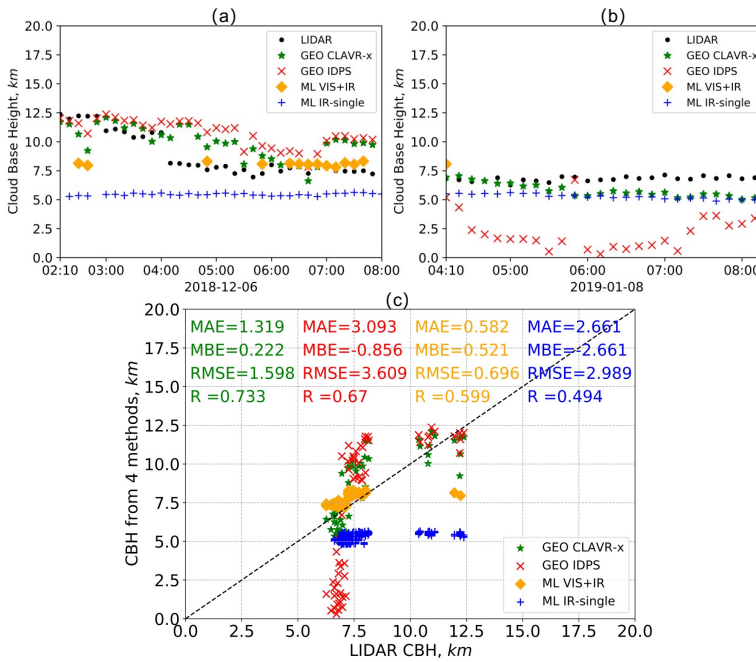


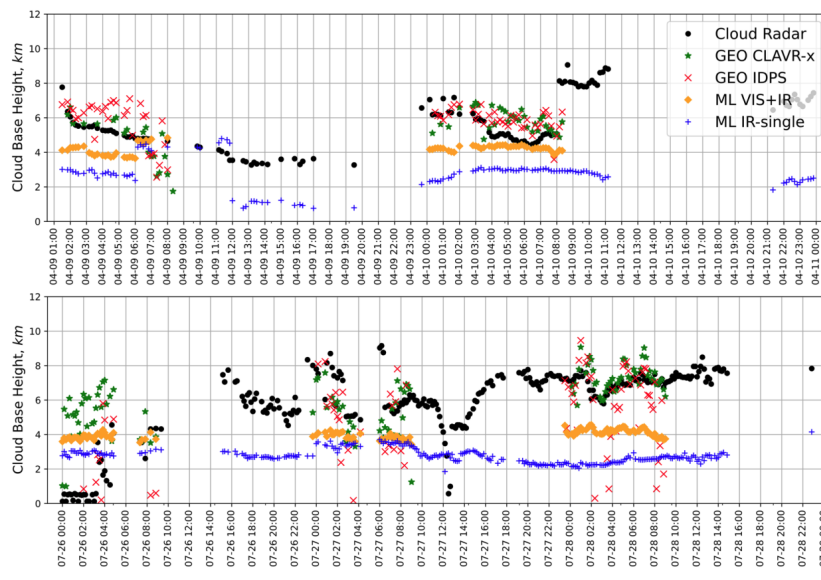
**Figure 5.** Comparisons of the CBHs from the ground-based lidar measurements (black solid circle) at Yunnan Lijiang station and the four GEO satellite retrieval algorithms, namely the GEO IDPS (red cross symbol), the GEO CLAVR-x (green solid asterisk), the ML-based VIS+IR model (orange solid diamond) and the ML-based IR-single model (blue plus sign) algorithms. Fig 5a and 5b show the time series of CBHs from lidar and the four GEO satellite retrieval algorithms on December 6, 2018 and January 8, 2019, respectively. Fig 5c shows the scatterplots of CBH samples from the lidar measurements and the four retrieval algorithms.

删除了: 6

删除了: 6

删除了: 6

1286  
1287  
1288  
1289  
1290

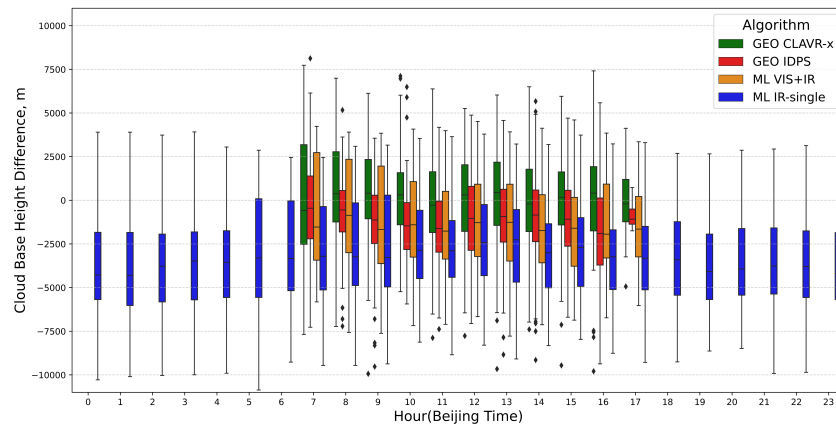


1291  
1292 **Figure 6.** Same as Figure 5, but for the CBH sample results from the cloud radar at  
1293 Beijing Nanjiao station (black solid circle) on April 9–10, 2017 (top panel) and July  
1294 26–28, 2017 (bottom panel).

1295  
1296  
1297  
1298  
1299  
1300  
1301  
1302  
1303  
1304

删除了：..

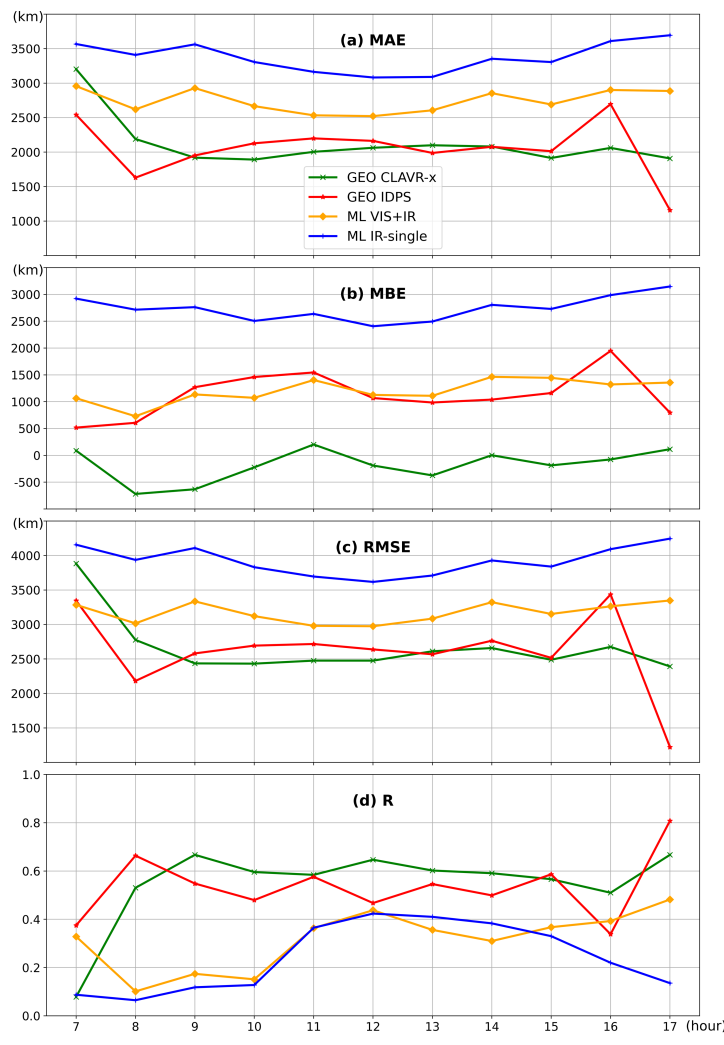
1306  
1307  
1308  
1309  
1310  
1311  
1312



1313  
1314 **Figure 7.** Box plots of the hourly CBH errors of four GEO satellite retrieval  
1315 algorithms (GEO IDPS, GEO CLAVR-x, ML-based VIS+IR and ML-based IR-single)  
1316 relative to the CBHs from the cloud radar at Beijing Nanjiao station in 2017. The box  
1317 symbols signify the 25th, 50th and 75th percentiles of errors. The most extreme  
1318 sample points between the 75th and outlier, and the 25th percentiles and outliers are  
1319 marked as whiskers and diamonds, respectively. Except for the period between 7 and  
1320 17 UTC (local time), the three algorithms of GEO CLAVR-x, GEO IDPS, and ML  
1321 VIS+IR are unavailable due to the lack of reflected solar radiance measurements.

1322  
1323  
1324  
1325  
1326  
1327  
1328  
1329  
1330  
1331

1332  
1333  
1334  
1335  
1336  
1337  
1338



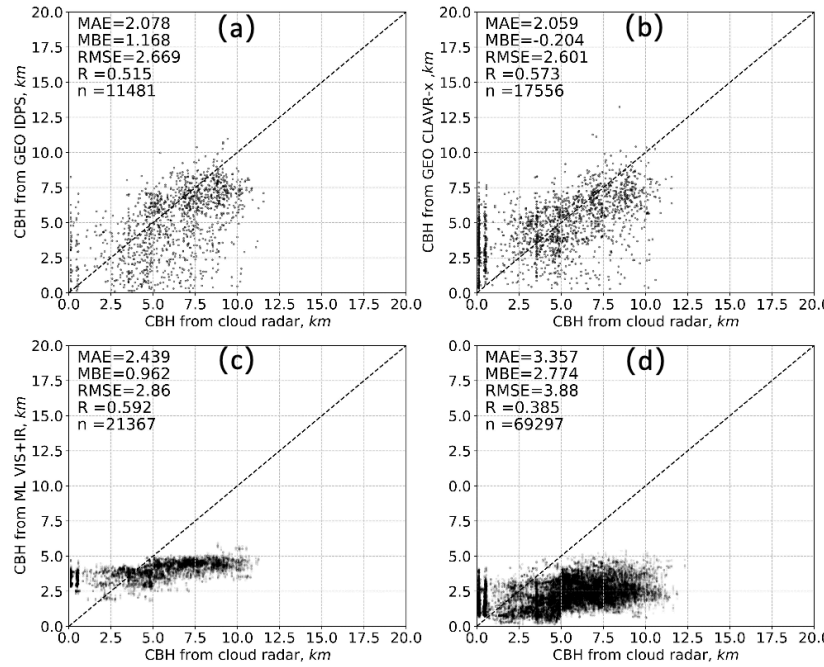
1339  
1340 **Figure 8.** Comparisons of hourly (a) MAE, (b) MBE, (c) RMSE, and (d) R of CBH  
1341 (relative to the CBHs from the cloud radar at Beijing Nanjiao station) from 07 to 17  
1342 (local time) between four retrieval algorithms (GEO IDPS, GEO CLAVR-x,

1343 ML-based VIS+IR and ML-based IR-single) in 2017.

1344

1345

1346



1347

1348 **Figure 9.** Comparisons between the CBHs from the cloud radar at Beijing Nanjiao  
1349 station and the matched CBHs from the four retrieval algorithms (GEO IDPS, GEO  
1350 CLAVR-x, ML-based VIS+IR and ML-based IR-single) in 2017.

1351

1352

1353

1354

1355

1356